

Duality in spatially resolved star-formation relations in local LIRGs

M. Sánchez-García¹, M. Pereira-Santaella¹, S. García-Burillo², L. Colina¹, A. Alonso-Herrero³, M. Villar-Martín¹, T. Saito^{4,5}, T. Díaz-Santos^{6,7}, J. Piqueras López¹, S. Arribas¹, E. Bellocchi³, S. Cazzoli⁸, and A. Labiano^{3,9}

¹ Centro de Astrobiología (CSIC/INTA), Ctra de Torrejón a Ajalvir, km 4, 28850 Torrejón de Ardoz, Madrid, Spain
e-mail: mariasg@cab.inta-csic.es

² Observatorio Astronómico Nacional (OAN-IGN)-Observatorio de Madrid, Alfonso XII, 3, 28014 Madrid, Spain

³ Centro de Astrobiología (CAB, CSIC-INTA), ESAC Campus, E-28692 Villanueva de la Cañada, Madrid, Spain

⁴ Department of Physics, General Studies, College of Engineering, Nihon University, 1 Nakagawara, Tokusada, Tamuramachi, Koriyama, Fukushima 963-8642, Japan

⁵ National Astronomical Observatory of Japan, 2-21-1 Osawa, Mitaka, Tokyo 181-8588, Japan

⁶ Department of Physics, University of Crete, GR-71003, Heraklion, Greece

⁷ Institute of Astrophysics, Foundation for Research and Technology-Hellas, Heraklion, GR-70013, Greece

⁸ Instituto de Astrofísica de Andalucía (IAA-CSIC), Apdo. 3004, E-18008 Granada, Spain

⁹ Telespazio UK for the European Space Agency (ESA), ESAC, Spain

ABSTRACT

We analyse the star formation (SF) relations in a sample of 16 nearby luminous infrared galaxies (LIRGs) with more than 2800 regions defined on scales of 90 to 500 pc. We used ALMA to map the distribution of the cold molecular gas traced by the J = 2–1 line of CO and archival Pa α HST/NICMOS imaging to trace the recent SF. In four objects, we find two different branches in the Kennicutt-Schmidt relation at 90 pc scales, suggesting the existence of a duality in this relation. The two branches correspond to two different dynamical environments within each galaxy. One branch, which corresponds to the central region of these galaxies (90% of the regions are located at radii <0.85 kpc), shows higher gas and star formation rate surface densities with higher velocity dispersion. The other branch, which shows lower molecular gas and SF rate surface densities, corresponds to the more external disk regions (r~1 kpc). Despite the scatter, the SF efficiency of the galaxies with a dual behaviour increases with increasing boundedness as measured by the *b* parameter ($b \equiv \Sigma_{H2}/\sigma^2 \propto \alpha_{vir}^{-1}$). At larger spatial scales (250 and 500 pc), the duality disappears. The rest of the sample does not show evidence of this dual behaviour at any scale.

Key words. galaxies: star formation – infrared: galaxies – galaxies: ISM

1. Introduction

The relationship between the rate at which stars form and the amount of gas contained in galaxies is commonly referred to as the star formation (SF) law or as the Kennicutt-Schmidt (KS) relation (Schmidt 1959; Kennicutt 1998). This relation is expressed as

$$\Sigma_{SFR} \propto \Sigma_{gas}^N \quad (1)$$

where Σ_{SFR} and Σ_{gas} are the star formation rate (SFR) and molecular gas surface densities, respectively, and *N* the power-law index. This relation was initially studied in spatially unresolved observations of galaxies, finding a power-law index of 1.4-1.5 (Kennicutt 1998; Yao et al. 2003). The physical processes that explain the observed power-law index are not clear yet. More recently, a duality has been found in the SF laws when normal and starburst galaxies are considered (Daddi et al. 2010; Genzel et al. 2010; García-Burillo et al. 2012). In these studies, normal galaxies show depletion times ($t_{dep} = M_{H2}/SFR$) between 4 and 10 times longer than starbursts. This duality introduces a discontinuity in the KS relation. In this case, when each galaxy population (normal and starbursts) is treated independently, there is a linear relation ($N \sim 1$).

Spatially resolved KS relation studies ($\lesssim 1$ kpc) (e.g., Leroy et al. 2008; Casasola et al. 2015; Pereira-Santaella et al. 2016b; Williams et al. 2018; Viaene et al. 2018) found a wide range of

N values ($N \approx 0.6-3$) with a considerable scatter in the relation (0.1-0.4 dex). These results suggest that there is a breakdown in the star-formation law at sub-kpc scales ($\lesssim 300$ pc), although the correlation is restored at larger spatial scales (Onodera et al. 2010; Schruba et al. 2010). This breakdown may be due to the different evolutionary states of individual giant molecular clouds within the galaxies when resolved at sub-kpc scales. In addition to the relation between Σ_{SFR} and Σ_{gas} , other parameters, such as the velocity dispersion (σ) or boundedness of the gas ($b \equiv \Sigma_{gas}/\sigma^2 \propto \alpha_{vir}^{-1}$, where α_{vir} is the virial parameter), have been studied to characterize the local dynamical state of the gas (e.g., Leroy et al. 2017; Sun et al. 2018). These studies suggest that the dynamical environment plays an important role in the ability to form stars within a galaxy.

These previous sub-kpc studies focused on nearby normal and active galactic nuclei (AGN) galaxies. However, more intense local starburst galaxies (i.e., luminous and ultraluminous infrared galaxies; LIRGs and ULIRGs) have been barely studied at sub-kpc scales (e.g., Xu et al. 2015; Pereira-Santaella et al. 2016b; Paraficz et al. 2018; Saito et al. 2016). In this work, we present a detailed analysis of the SF relations at cloud scales (~ 100 pc) in a sample of 16 local LIRGs.

2. The sample

We present new sub-kpc CO(2–1) observations obtained by the Atacama Large Millimeter Array (ALMA) of a representative sample of 16 local LIRGs. Our sample is drawn from the volume-limited sample of 34 local LIRGs ($40 \text{ Mpc} < D < 75 \text{ Mpc}$) defined by Alonso-Herrero et al. (2006) and contains 85% of their southern targets which can be observed with ALMA. Our sample contains six isolated galaxies, six pre-coalescence systems (interacting galaxies and pairs of galaxies), and four merger objects (Yuan et al. 2010; Rich et al. 2012; Bellocchi et al. 2013). Eight objects are classified as AGN in the optical and/or show evidence of AGN activity from mid-infrared diagnostics (Alonso-Herrero et al. 2012). In Table 1 we present the main properties of the individual galaxies of the sample.

3. Observations and data reduction

3.1. CO(2–1) ALMA data

We used ALMA Band 6 CO(2–1) observations carried out between August 2014 and August 2018 from several projects (see Table 2). The observations were obtained using a combination of extended and compact antenna array configurations, except in the case of the two galaxies part of project 2017.1.00395.S which only used an extended antenna array configuration. The integration time of the sources ranges between ~ 7 to ~ 34 min. We calibrated the data using the standard ALMA reduction software CASA¹ (McMullin et al. 2007). We subtracted the continuum emission in the uv plane using an order 0 baseline. For the cleaning, we used the Briggs weighting with a robustness parameter of 0.5 (Briggs 1995), providing a spatial resolution of 48–106 pc ($0.19''$ – $0.37''$). The maximum recoverable scales (MRS) for the compact+extended configuration data range between $\sim 8''$ and $\sim 11''$ (1.7–2.3 kpc). In the case of the only extended configuration observations, the MRS is $\sim 3''$ (1.1 kpc). In this paper, we study spatial scales between 90 and 500 pc, which are 2 to 25 times smaller than the MRS, so we expect that the missing flux due to the absence of short spacing is low at these scales. In addition, for two of these systems with single-dish CO(2–1) observations, the integrated ALMA and single-dish fluxes agree within 15% (Pereira-Santaella et al. 2016b,a).

The final data cubes have channels of 7.8 MHz ($\sim 10 \text{ km s}^{-1}$) for the sample, except ESO320-G030 and NGC 5135, which have channels of ~ 4 MHz ($\sim 5 \text{ km s}^{-1}$) and ~ 23 MHz ($\sim 30 \text{ km s}^{-1}$) respectively. The field of view (FoV) of the ALMA single pointing data has a diameter of $\sim 24''$ (~ 5 –8 kpc). The three mosaics (MCG-02-33-098, NGC 3256 and NGC 7469) have a diameter between ~ 38 and $\sim 48''$ (~ 11 and 17 kpc). We applied the primary beam correction to the data cubes. Further details on the observations for each galaxy are listed in Table 2.

A common spatial scale of about 70–90 pc was defined to have a homogeneous data set. We convolved to 80 pc the data cubes of the galaxies with spatial resolutions better between 48 and 68 pc (ESO297-G011, NGC1614, NGC2369, NGC3256, ESO320-G030 and NGC7469). For the remaining objects, we directly used cleaned data cubes with spatial resolutions between 72 and 89 pc. For NGC 7130 the original spatial resolution was ~ 110 pc. We used this slightly larger spatial scale for the SF law in this galaxy. We obtained the CO(2–1) moment 0 and 2 maps by doing the following: to identify the CO(2–1) emission in each channel of data cube, we selected pixels with fluxes $> 5\sigma_{CO}$. We

estimated the sensitivity σ_{CO} in a spectral channel without evident CO(2–1) emission and with no primary beam correction. In addition to the $5\sigma_{CO}$ criterion, and to ensure that the emission of data cubes does not include noise spikes, we did not consider spatial pixels that have emission from less than three spectral channels. Finally, for each pixel meeting the above criteria, we expanded the spectral range to include a channel before and after the emission to ensure that line profile wings below $5\sigma_{CO}$ are also considered. In addition to the nominal 90 pc resolution, we smoothed the data to 240 and 500 pc resolutions to study the effect of the spatial scale on the SF laws.

3.2. Ancillary HST/NICMOS data

We used the continuum subtracted near-infrared narrow-band Pa α 1.87 μm images taken with the NICMOS instrument on board the Hubble Space Telescope (HST) to map the distribution of recent star formation in the galaxies of the sample (see Alonso-Herrero et al. 2006).

We downloaded the raw data from the *Hubble* Legacy Archive (HLA)². The individual frames were combined using the PyDrizzle package with a final pixel size ($0.03''$) half of the original to improve the spatial sampling. The FoV of the images is approximately $19''.5 \times 19''.5$ (~ 4.2 –7.4 kpc). To obtain the final images, we subtracted the background emission and corrected the astrometry using stars within the NICMOS FoV in the F110W ($\lambda_{\text{eff}} = 1.13 \mu\text{m}$) or F160W ($\lambda_{\text{eff}} = 1.60 \mu\text{m}$) filters and the Gaia DR2 catalogue³. Three objects (ESO297-G011, MCG-02-33-098 E/W, and IC4518 E) do not have Gaia stars in their NICMOS images FoV. In these cases, we adjusted the astrometry using likely NICMOS counterparts of the regions detected in the ALMA continuum and CO(2–1) maps. After that, the images were rotated to have the standard north-up, east-left orientation. The Pa α maps (spatial resolutions of 25–50 pc) were convolved with a Gaussian kernel to match the angular resolution of the ALMA maps.

3.3. Region selection

We defined circular apertures centred on local maxima in the CO(2–1) moment 0 maps with a diameter of 90 pc, 240 pc and 500 pc, depending on the spatial resolution of the maps. To do so, we first sorted the CO moment 0 pixel intensities. Then, we defined circular regions using as centre the pixels in descending intensity order preventing any overlap between the regions. With this method, we end up having independent non-overlapping regions centred on local emission maxima that cover all the CO emission in each galaxy. In total, we defined 4802 regions for the whole sample.

We estimated the cold molecular gas mass using the Galactic CO-to-H₂ conversion factor, $\alpha_{CO}^{1-0} = 4.35 \text{ M}_{\odot}/\text{K}/(\text{km/s})/\text{pc}^2$ (Bolatto et al. 2013) and the CO(2–1)/CO(1–0) ratio (R_{21}) of 0.7 obtained from the single-dish CO data of LIRG IC4687 (Albrecht et al. 2007). The R_{21} value used is within the range found by Garay et al. (1993) in infrared galaxies and is similar to the one found by Leroy et al. (2013) in nearby spiral galaxies. We explore the variation of the CO-to-H₂ conversion factor in Sect. 3.5. We calculated the molecular gas mass surface density (Σ_{H_2}) taking into account the area of the selected regions.

Once we have the regions in CO(2–1) emission maps, we selected the regions in the Pa α maps. These regions are at the

² <http://hla.stsci.edu/hlview.html>

³ <http://www.cosmos.esa.int/web/gaia/dr2>

¹ <http://casa.nrao.edu/>

Table 1. The Volume Limited Sample of Local LIRGs

Object		α	δ	z	D_L	i	$\log L_{IR}$	Morf.	Spectral Class	Ref.
Galaxy Name	IRAS Name	J2000.0	J2000.0							
(1)	(2)	[h m s]	[° ′ ″]	(5)	[Mpc]	[°]	[L_\odot]	(9)	(10)	(11)
ESO 297-G011	F01341-3735 N	01 36 23.40	-37 19 17.6	0.0168	73.4	38 ± 11	11.13	1	HII	1,2
NGC 1614	F04315-0840	04 33 59.85	-08 34 44.0	0.0159	69.7	48 ± 2	11.61	2	composite	3
NGC 2369	F07160-6215	07 16 37.73	-62 20 37.4	0.0111	49.7	66 ± 6	11.18	0	composite	4
NGC 3110	F10015-0614	10 04 02.11	-06 28 29.2	0.0163	79.8	57 ± 3	11.37	0	HII	2,3
NGC 3256	F10257-4339	10 27 51.27	-43 54 13.5	0.0093	45.7	-	11.72	2	HII	5
ESO 320-G030	F11506-3851	11 53 11.72	-39 07 48.9	0.0102	52.2	56 ± 4	11.36	0	HII	4,6
MCG-02-33-098 W	F12596-1529	13 02 20.00	-15 46 03.7	0.0156	75.2	54 ± 6	11.19	1	composite	2
MCG-02-33-098 E	F12596-1529	13 02 20.38	-15 45 59.7	0.0159	75.2	39 ± 1	11.11	1	HII	2,3,7
NGC 5135	F13229-2934	13 25 44.06	-29 50 01.2	0.0136	64.8	53 ± 9	11.33	0	Sy2	1,2,3,9,10
IC 4518 W	F14544-4255	14 57 41.18	-43 07 55.6	0.0160	74.6	50 ± 4	11.16	1	Sy2	2,8
IC 4518 E	F14544-4255	14 57 44.46	-43 07 52.9	0.0154	71.2	75 ± 2	11.12	1	-	4
...	F17138-1017	17 16 35.79	-10 20 39.4	0.0172	76.7	50 ± 1	11.39	2	composite/HII	2
IC 4734	F18341-5732	18 38 25.70	-57 29 25.6	0.0154	68.5	58 ± 10	11.28	0	HII	2
NGC 7130	F21453-3511	21 48 19.52	-34 57 04.5	0.0160	67.6	50 ± 9	11.33	2	Sy2	3,8,9,10
IC 5179	F22132-3705	22 16 09.10	-36 50 37.4	0.0112	46.7	62 ± 5	11.13	0	HII	3,7
NGC 7469	F23007+0836	23 03 15.62	+08 52 26.4	0.0160	66.7	39 ± 5	11.54	1	Sy1	8,9,10,11

Notes. Col. (1): Galaxy name. Col. (2): IRAS denomination from Sanders et al. (2003). Col. (3) and (4): right ascension (hours, minutes, seconds) and declination (degrees, arcminutes, arcseconds) from the NASA Extragalactic Database (NED), respectively. Col (5): redshift. Col. (6): Luminosity distance from NED. Col. (7): Inclination. Col. (6): Infrared luminosity ($L_{IR}(8-1000) \mu\text{m}$) calculated from the IRAS flux densities f_{12} , f_{25} , f_{60} , and f_{100} (Sanders et al. 2003). Col. (8): Morphological class (0 identifies *isolated* objects, 1 *pre-coalescence* systems, and 2 stands for *merger* objects. Col. (9): Nuclear activity class (HII= HII region-like, Sy2=Seyfert 2 y Sy1=Seyfert 1, composite). Col. (10): References of the nuclear classification: 1: Kewley et al. (2001); 2: Corbett et al. (2003); 3:Yuan et al. (2010); 4:Pereira-Santaella et al. (2011); 5: Lípari et al. (2000); 6: van den Broek et al. (1991); 7: Veilleux et al. (1995); 8:Pereira-Santaella et al. (2010); 9: Alonso-Herrero et al. (2012); 10: Alonso-Herrero et al. (2009); 11: Petric et al. (2011).

Table 2. CO(2–1) observations of the sample.

Object		$\theta_{maj} \times \theta_{min}$	θ_m	P.A.	Sensitivity	Project	Mosaics	MRS	SINFONI
Galaxy Name	IRAS Name	[″] [″]	[″, pc]	[°]	[mJy beam ⁻¹]	PI	(8)	[″]	
(1)	(2)	(3)	(4)	(5)	(6)	(7)	(8)	(9)	
ESO 297-G011	F01341-3735	0.21×0.16	0.19, 67	-72	0.53	MPS		9.4	
NGC 1614	F04315-0840	0.22×0.15	0.19, 62	-74	0.43	MPS		10.8	
NGC 2369	F07160-6215	0.24×0.21	0.22, 53	88	0.51	MPS		8.8	✓
NGC 3110	F10015-0614	0.26×0.21	0.23, 89	-83	0.35	MPS		8.8	✓
NGC 3256	F10257-4339	0.23×0.21	0.22, 48	63	0.43	KS	✓	5.4	✓
ESO 320-G030	F11506-3851	0.30×0.24	0.27, 68	63	0.89	LC1		8.7	✓
MCG-02-33-098 W	F12596-1529	0.23×0.17	0.20, 73	89	0.48	MPS	✓	9.4	
MCG-02-33-098 E	F12596-1529	0.23×0.17	0.20, 72	89	0.48	MPS	✓	9.4	
NGC 5135	F13229-2934	0.31×0.22	0.26, 82	63	0.21	LC2		9.4	✓
IC 4518 W	F14544-4255	0.23×0.20	0.21, 75	-86	0.46	MPS		10.3	
IC 4518 E	F14544-4255	0.23×0.20	0.21, 73	-87	0.47	MPS		10.3	
...	F17138-1017	0.26×0.22	0.24, 87	-62	0.75	MPS		7.6	✓
IC 4734	F18341-5732	0.25×0.21	0.23, 75	-73	0.77	TDS		2.7	
NGC 7130	F21453-3511	0.36×0.29	0.32, 105	69	0.29	MPS		9.9	✓
IC 5179	F22132-3705	0.40×0.34	0.37, 82	44	0.45	MPS		9.8	✓
NGC 7469	F23007+0836	0.23×0.18	0.21, 65	-39	0.29	TDS	✓	2.8	

Notes: Col. (1): Galaxy name. Col. (2): IRAS denomination from Sanders et al. (2003). Col. (3): major (θ_{maj}) and minor (θ_{min}) FWHM beam sizes. Col. (4): mean FWHM beam size (θ_m) in arcseconds and parsecs, respectively. Col. (5): position angle (P.A.) in degrees. Col. (6): 1σ line sensitivity of the CO(2–1) observations. Col. (7): Principal investigator of the ALMA project: MPS: Miguel Pereira-Santaella (2017.1.00255.S), KS: Kazimierz Sliwa (2015.1.00714.S), LC1: Luis Colina (2013.1.00271.S), LC2: Luis Colina (2013.1.00243.S) and TDS: Tanio Díaz-Santos (2017.1.00395.S). Col. (8): ✓ galaxies with mosaics data. Col. (9): Maximum recoverable scales. Col. (10): ✓ galaxies with SINFONI data.

same spatial coordinates as the CO(2–1) regions. In this case, we considered Pa α detections when the line emission is above $3\sigma_{Pa\alpha}$. The $\sigma_{Pa\alpha}$ in these images corresponds to the background noise. The regions that are below 3σ correspond to the upper limits. Pa α emission is detected in 2783 regions (58% of the to-

tal). Then, we estimated the SFR surface density (Σ_{SFR}) of the regions. We used the H α Kennicutt & Evans (2012) calibration, which assumes a Kroupa (2001) initial mass function, and an H α /Pa α ratio of 8.6 (case B at $T_e=10,000$ K and $n_e = 10^4 \text{ cm}^{-3}$, Osterbrock & Ferland 2006). The variation of this ratio is $\sim 15\%$

due to changes in the physical properties of the ionized gas (i.e., $T_e = 5\text{--}20 \times 1000$ K and $n_e = 10^2\text{--}10^6$ cm $^{-3}$). We took into account the area of the selected regions, obtaining the SFR surface density. All these Σ_{H_2} and Σ_{SFR} values are corrected for the inclination of each galaxy (see Table 1).

Both the SFR and the cold molecular gas surface density estimates are affected by the flux calibration errors. We assume an uncertainty of about 10% in the ALMA data (see ALMA Technical Handbook⁴), and $\sim 15\text{--}20\%$ in the case of NICMOS data (Alonso-Herrero et al. 2006; Böker et al. 1999).

3.4. Extinction correction

To correct the Pa α emission for extinction, we used the Br δ and Br γ line maps observed at 240 pc scales with the SINFONI instrument on the Very Large Telescope (VLT) in eight objects from our sample (effective FoV between $8'' \times 8''$ and $12'' \times 12''$; Piqueras López et al. 2013) to derive A_K (see Table 2). We calculated the Br δ /Br γ ratio in circular regions with a diameter of 240 pc. We assumed an intrinsic Br δ /Br γ ratio of 1.52 (Hummer & Storey 1987) and the Fitzpatrick (1999) extinction law. In each 240 pc region, we determined A_K ($A_K = 0.11 \times A_V$) and the column density from the CO(2–1) 240 pc maps (N_{H_2}).

The N_{H_2} values were divided in five equally spaced ranges between $\log N_{H_2}/\text{cm}^{-2} = 22.55$ and 23.88. For each range, we estimated the mean and standard deviation of A_K obtaining slightly increasing values with N_{H_2} , between 0.95 ± 0.6 and 1.98 ± 1.29 mag. To obtain an estimation of the extinction, we measured N_{H_2} in the circular apertures with a diameter of 90 (110), 240 and 500 pc in our entire sample and assigned them the mean A_K corresponding to their N_{H_2} range. We assume that the galaxies without SINFONI data (half of the sample) follow the same trend found between A_K and N_{H_2} in the other eight galaxies.

3.5. The effects of CO-to- H_2 conversion factor

The obtained cold molecular gas masses depend on the conversion factor (α_{CO}) used. In this paper we assume a Galactic α_{CO} conversion factor to derive molecular gas masses. As argued in the following, we do not expect that a lower conversion factor, typical of ULIRGs (Papadopoulos et al. 2012) is appropriate for our targets.

Our sample does not contain strongly interacting objects or compact mergers like most local ULIRGs. The galaxies of our sample have a mean infrared luminosity of $\log(L_{IR}/L_\odot) = 11.30$. In addition, galaxies of our sample show a mean effective radius of the molecular component (R_{CO}^{eff}) of 740 pc (Bellocchi et al. in prep), while local ULIRGs show a mean value of $R_{CO}^{eff} = 340$ pc (Pereira-Santaella et al. 2021). Therefore, it is likely that α_{CO} of our sample differs from that of local ULIRGs.

The CO-to- H_2 conversion factor can be affected by the metallicity of the galaxies, showing higher values with decreasing metallicity ($\alpha_{CO} = 4.35 (Z/Z_\odot)^{-1.6} M_\odot \text{pc}^{-2} (\text{K km s}^{-1})^{-1}$, Accurso et al. 2017). Rich et al. (2012) studied the metallicity in some local (U)LIRGs, showing a decrease in the abundance with increasing radius. In the case of the metallicity in local disks, Sánchez et al. (2014) observed a similar behaviour. Based on these works, the expected variation of the conversion factor due to metallicity gradients at $r < 4$ kpc is small, 20–30%.

⁴ <http://almascience.eso.org/documents-and-tools/latest/documents-and-tools/cycle8/alma-technical-handbook>

4. Results and discussion

4.1. The star formation relation for individual galaxies

We studied the molecular KS relation for each LIRG at scales of 90 (110) pc. As an example, Fig. 1 shows the SFR surface density as a function of molecular gas surface density for NGC 7130 (similar figures for the rest of the sample are presented in Appendix A.1). The KS diagram suggests that the regions follow two different power-laws. These two branches were identified using the Multivariate Adaptive Regression Splines (MARS) fit (Friedman 1991) in $\log \Sigma_{SFR}$ and $\log \Sigma_{H_2}$, which gives the position of the breaking points (cut-points) for a linear regression with multiple slopes. We obtained the adjusted coefficient of determination, the cut-points, and their errors using MARS fit in 100 realizations of the data based on the uncertainties in both axes.

We consider that the MARS breaking point is significant when the adjusted coefficient of determination found by MARS (\bar{R}_{MARS}^2) is larger than that of the linear fit (\bar{R}_{linear}^2). The adjusted coefficient of determination is used to compare the linear and MARS fits since it takes into account both the number of terms in the model and the number of data points. In this galaxy, the break of a linear regression occurs at $\log \Sigma_{H_2}/(M_\odot \text{yr}^{-1} \text{kpc}^{-2}) = 3.35$ (for cut on Σ_{SFR} , see Figure A.1).

We fit the two branches using the orthogonal distance regression (ODR) method. This fit gives power-law indices of $N = 4.19 \pm 0.46$ and $N = 0.68 \pm 0.07$. The *right* panel of Fig. 1 shows that the branch with higher gas and SFR densities (*left* panel) is located in the central region of the galaxy (at radii up to 0.85 kpc), while the other branch with lower gas and SFR densities is located in the more external disk regions. The duality is reinforced if we consider a factor $\alpha_{CO} = 0.8$ (Downes & Solomon 1998) typical of ULIRGs in the central regions of our galaxies.

We do not include in our analysis the upper limits. Pessa et al. (2021) studied the influence of the non-detections in several resolved scaling relations. In general, the non-detections could artificially flatten the relations at small spatial scales, resulting in a steepening when the analysis is carried out at larger spatial scales compared to the small scales. This is because the pixels with signal are averaged with the non-detection pixels at larger scales. However, they obtained that the no consideration of the non-detections in the star formation relation has a small impact on the measured slope.

4.2. The star-formation relation across the sample

We repeated the same analysis for the rest of the sample finding two different regimes (branches) in the KS relations in four galaxies (25% of the sample; dual galaxies hereafter; see Table 3 and Fig. A.2). At larger spatial scales (240 and 500 pc), the duality disappears and a standard single power-law KS relation is recovered (see Fig. 3).

The remaining twelve galaxies (75% of the sample) can be modelled with a single power-law (non-dual galaxies hereafter; see Table 4 and Fig. A.3) at 90 pc scales.

For the four dual galaxies, the cut-points on both the Σ_{H_2} and Σ_{SFR} axes are similar ($\log \Sigma_{H_2}/(M_\odot \text{pc}^{-2}) \approx 3.25$ and $\log \Sigma_{SFR}/(M_\odot \text{yr}^{-1} \text{kpc}^{-2}) \approx 0.91$).

Therefore, in the *top left* and *top middle* panels of Fig. 2, we combine all the regions of the dual galaxies with a cut on both axes obtained in each individual dual galaxy. We find that the power-law for the regions above the cut-points (hereafter referred to as high-N regions) is steeper than for the regions

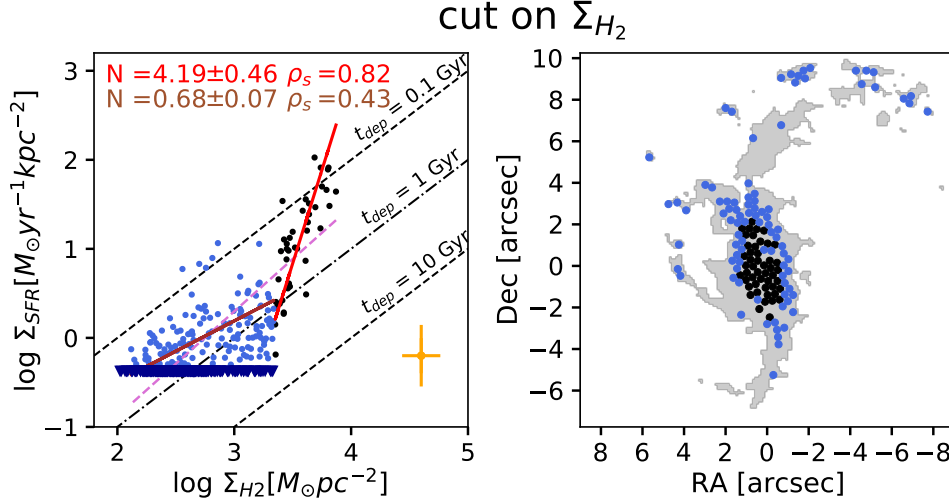


Fig. 1. *Left panel:* SFR surface density (Σ_{SFR}) as a function of the molecular gas surface density (Σ_{H_2}) derived from CO(2–1) in NGC 7130 at 110 pc scale. The blue and black points show the two branches derived applying the MARS method with breaking points in the $\log \Sigma_{H_2}$ axis. The black dashed lines mark constant depletion times ($t_{dep} = \Sigma_{H_2}/\Sigma_{SFR}$). The red and brown solid lines are the best fit for each branch. We indicate the Spearman’s rank correlation coefficients (ρ_s) and the power-law indices (N) of the derived best-fit KS relations. The pink dashed line is the best fit for whole points. The inverted triangles indicate upper limits. The errorbars indicate the mean systematic uncertainties in Σ_{H_2} of ± 0.14 dex (horizontal) and the extinction correction in Σ_{SFR} of ± 0.21 dex (vertical). *Right panel:* Location of the regions on the CO(2–1) map (grey). The black and blue circles correspond to regions in each of the two branches.

Table 3. Statistical parameters for dual galaxies.

galaxies	\bar{R}_{linear}^2	cut on $\log_{10}\Sigma_{H_2}$		cut on $\log_{10}\Sigma_{SFR}$	
		cut-point	\bar{R}_{MARS}^2	cut-point	\bar{R}_{MARS}^2
NGC 1614	0.69	3.31 \pm 0.12	0.75 \pm 0.04	1.68 \pm 0.32	0.71 \pm 0.03
NGC 3110	0.36	3.21 \pm 0.15	0.50 \pm 0.08	0.81 \pm 0.11	0.49 \pm 0.07
NGC 7130	0.49	3.35 \pm 0.11	0.71 \pm 0.05	0.53 \pm 0.15	0.52 \pm 0.03
IC 5179	0.48	3.12 \pm 0.18	0.62 \pm 0.05	0.61 \pm 0.37	0.52 \pm 0.03

Notes. The adjusted coefficient of determination (\bar{R}_{linear}^2) obtained by linear fit and the breaking point, the adjusted coefficient of determination (\bar{R}_{MARS}^2) obtained by MARS fit.

Table 4. Statistical parameters for the non dual galaxies

galaxies	\bar{R}_{linear}^2	cut on $\log_{10}\Sigma_{H_2}$		cut on $\log_{10}\Sigma_{SFR}$	
		cut-point	\bar{R}_{MARS}^2	cut-point	\bar{R}_{MARS}^2
ESO 297-G011	0.22	3.25 \pm 0.12	0.13 \pm 0.05	0.54 \pm 0.15	0.11 \pm 0.05
NGC 2369	0.63	3.45 \pm 0.20	0.60 \pm 0.03	0.62 \pm 0.22	0.60 \pm 0.04
NGC 3256	0.36	3.92 \pm 0.16	0.24 \pm 0.06	2.17 \pm 0.40	0.26 \pm 0.06
ESO 320-G030	0.18	2.89 \pm 0.10	0.17 \pm 0.03	0.95 \pm 0.12	0.16 \pm 0.05
MCG-02-33-098 W	0.65	3.50 \pm 0.13	0.63 \pm 0.05	1.72 \pm 0.29	0.64 \pm 0.04
MCG-02-33-098 E	0.27	3.02 \pm 0.14	0.11 \pm 0.05	0.95 \pm 0.15	0.08 \pm 0.03
NGC 5135	0.35	3.44 \pm 0.18	0.33 \pm 0.09	0.33 \pm 0.19	0.33 \pm 0.08
IC 4518 W	0.18	3.57 \pm 0.11	0.15 \pm 0.06	0.44 \pm 0.21	0.15 \pm 0.07
IC 4518 E	0.65	2.85 \pm 0.09	0.63 \pm 0.02	0.30 \pm 0.20	0.52 \pm 0.05
IRAS F17138-1017	0.50	2.75 \pm 0.21	0.46 \pm 0.07	0.21 \pm 0.18	0.47 \pm 0.05
IC 4734	0.79	3.55 \pm 0.14	0.83 \pm 0.05	1.24 \pm 0.29	0.81 \pm 0.04
NGC 7469	0.62	3.47 \pm 0.11	0.63 \pm 0.04	0.93 \pm 0.12	0.62 \pm 0.05

Notes. The adjusted coefficient of determination (\bar{R}_{linear}^2) obtained by linear fit, and the breaking point, the adjusted coefficient of determination (\bar{R}_{MARS}^2) obtained by MARS fit to the $\log_{10}\Sigma_{H_2}$ and $\log_{10}\Sigma_{SFR}$ axes in the KS relation for the non-dual galaxies.

below them (hereafter referred to as low-N regions). The indices of the best power-law fits are $N=4.12\pm 0.22$ (high-N regions) and $N=0.91\pm 0.04$ (low-N regions) when using the Σ_{H_2} cut-point (Fig. 2 top left) and $N=1.89\pm 0.15$ (high-N regions)

and $N=0.89\pm 0.03$ (low-N regions) when we consider the Σ_{SFR} cut-point (Fig. 2 top middle).

When we fit all the regions from the dual galaxies using the MARS method (Fig. 2 bottom row), we obtain a value of \bar{R}_{MARS}^2

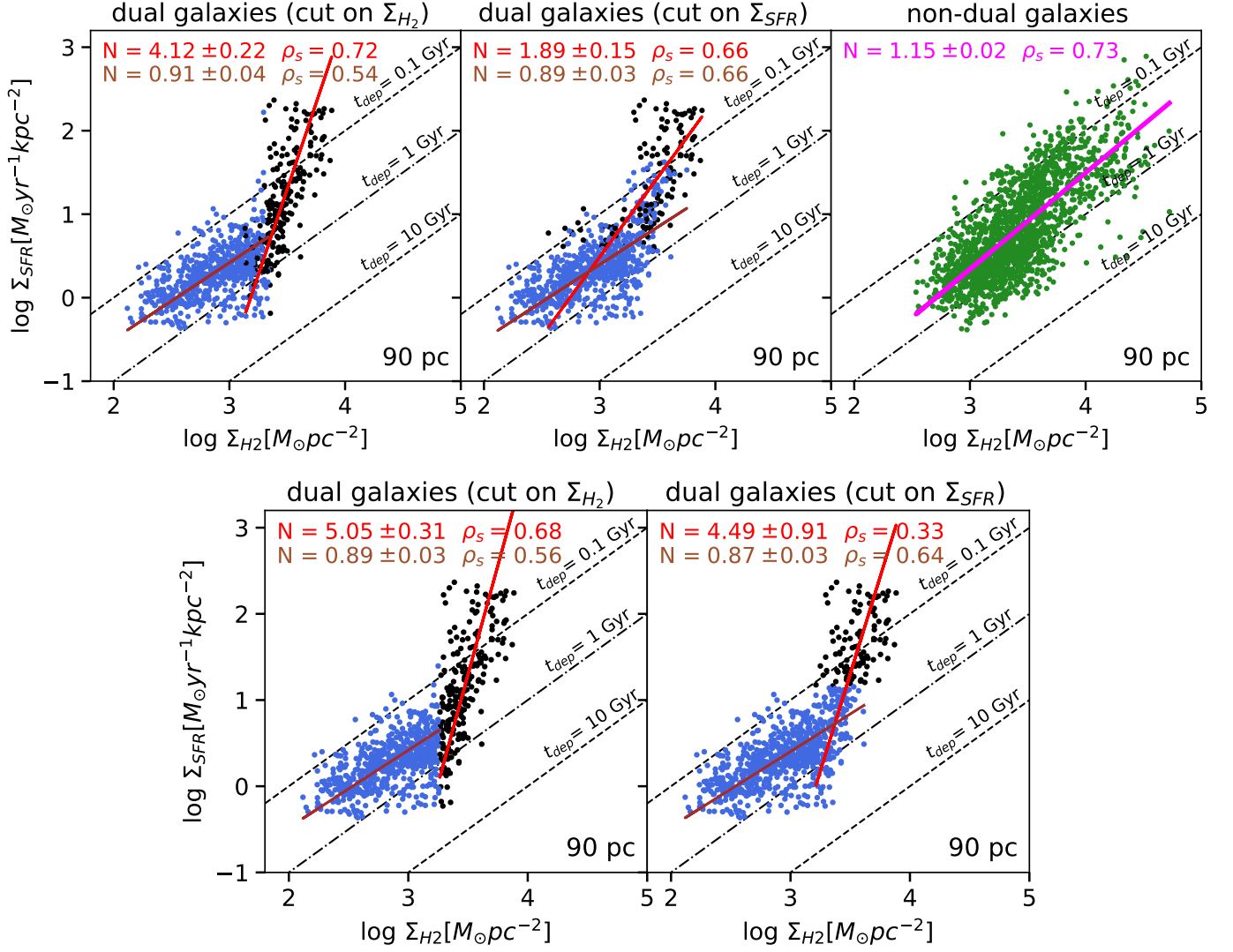


Fig. 2. SFR surface density as a function of the molecular gas surface density using 90 (110) pc regions. *Top left and top middle panels:* The black and blue points correspond to the two different regimes (branches) identified in the four dual galaxies using the MARS method in each individual galaxy. *Top right:* The green circles correspond to the regions in the remaining twelve galaxies. *Bottom row:* The black and blue points correspond to the two branches identified using the MARS method in all the regions from the dual galaxies. The red, brown, and magenta solid lines indicate the best fit for each regime. The dashed lines mark constant t_{dep} .

(0.67 ± 0.06 and 0.59 ± 0.03 on $\log_{10} \Sigma_{H_2}$ and $\log_{10} \Sigma_{SFR}$, respectively) higher than \bar{R}_{linear}^2 (0.55) and similar cut-point values to the ones in the individual dual galaxies ($\log \Sigma_{H_2} / (M_{\odot} \text{pc}^{-2}) = 3.27 \pm 0.17$ and $\log \Sigma_{SFR} / (M_{\odot} \text{yr}^{-1} \text{kpc}^{-2}) = 1.16 \pm 0.19$).

For the twelve non-dual galaxies, we find a single linear power-law with an index $N = 1.15 \pm 0.02$ (Fig. 2 *top right*). The dual and non-dual behaviours are also present before applying the extinction correction in Figure 4.

4.3. Radial distribution of the two regimes

To identify what causes the two branches in the SF laws for these four galaxies, we first investigate their spatial distribution. Fig. 5 shows the cumulative distribution of the molecular gas mass of the regions, based on the Σ_{H_2} cut selection, in the dual galaxies as a function of the radial distance. We find that the high-N regions are located in the central region of the galaxies, 50% (90%) at radii smaller than 0.50 kpc (0.85 kpc) from the centre. The molecular mass in the high-N regions follows the same ra-

dial distribution. The low-N regions are located at larger radii with a median radius of ~ 1 kpc and only $\sim 45\%$ of the regions are at radii lower than 0.88 kpc. We find the same trends using the cut on Σ_{SFR} .

4.4. Self-gravity of the gas

We explored the dynamical state of molecular gas in the regions using the boundedness parameter ($b \equiv \Sigma_{mol} / \sigma^2 \propto \alpha_{vir}^{-1}$, where σ is the velocity dispersion and α_{vir} the virial parameter). We obtained the velocity dispersion from the CO(2–1) moment 2. Fig. 6 shows the cold molecular gas depletion time ($t_{dep} = \Sigma_{H_2} / \Sigma_{SFR}$) as a function of the boundedness parameter (b) at 90 pc scales. Despite the scatter (~ 2.5 dex in t_{dep}), at these scales there is a weak trend with decreasing t_{dep} for increasing b in the dual galaxies (*top left*).

When we consider the low- and high-N regions separately (*bottom row*), we find that the high-N regions in both cuts show a slightly better correlation between t_{dep} and b ,

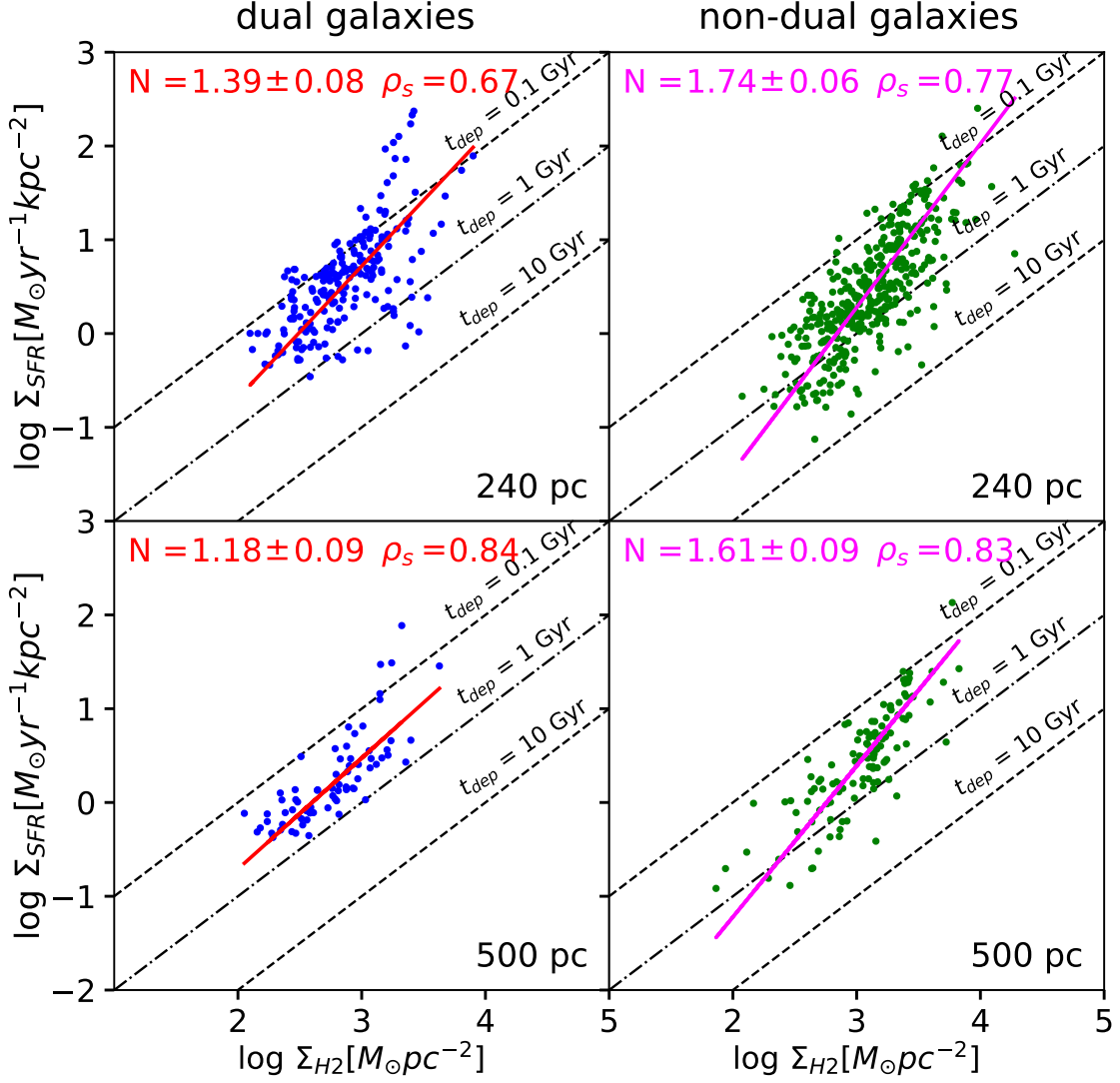


Fig. 3. SFR surface density as a function of the molecular gas surface density using 240 (*top row*) and 500 (*bottom row*) pc regions. The blue and green circles correspond to the regions of the galaxies with two regimes at 90 pc and the non-dual galaxies, respectively. The dark orange and magenta solid lines indicate the best fit. The dashed lines mark constant t_{dep} .

while for the low-N regions the trend disappears. The high-N regions show gas with larger b (with a mean b parameter of $\log b/M_{\odot}\text{pc}^{-2}(\text{km s}^{-1})^{-2} \approx 0.52$) and have shorter t_{dep} in both cuts than the low-N regions (with a mean b of $\log b/M_{\odot}\text{pc}^{-2}(\text{km s}^{-1})^{-2} \approx 0.30$). The non-dual galaxies do not show a clear relation. Table 5 summarizes the correlations.

Leroy et al. (2017) found, from the intensity weighted average on scales of 40 pc within regions of 370 pc, that gas with larger b (more bound) exhibits shorter t_{dep} in the spiral galaxy M51. This means that when b increases the system is more gravitationally bounded. However, Kreckel et al. (2018) did not find any correlation between b and t_{dep} in another spiral (NGC 628) at 50 pc scales within 500 pc regions, which is in agreement with our results for the non-dual galaxies and the low-N regions in dual galaxies. For the high-N regions in the dual galaxies, t_{dep} seems to decrease for increasing b although the scatter is large. The depletion times in our sample are between 4-8 times shorter than in these two spirals. This difference is consistent with what was found in previous works for starbursts (Daddi et al. 2010; Genzel et al. 2010; García-Burillo et al. 2012). However, for sim-

ilar b , there is a factor of 10 in t_{dep} . As a consequence, it is not clear if a universal relation between t_{dep} and b exists.

4.5. Velocity dispersion of the gas

We explore the behaviour of the velocity dispersion in our sample. Fig. 7 shows the SF efficiency of the cold molecular gas ($\text{SFE} = \Sigma_{\text{SFR}}/\Sigma_{\text{H}_2}$) as a function of the velocity dispersion (σ). The velocity dispersion was obtained from the CO(2–1) moment 2. We find that the global mean values of the σ and SFE for the dual galaxies ($\log \sigma/\text{km s}^{-1} = 1.36 \pm 0.16$ and $\log \text{SFE}/\text{Myr}^{-1} = -2.56 \pm 0.26$) and for the non-dual galaxies ($\log \sigma/\text{km s}^{-1} = 1.41 \pm 0.18$ and $\log \text{SFE}/\text{Myr}^{-1} = -2.60 \pm 0.31$) are similar. However, when we consider the low- and high-N regions independently, the mean values are different. The high-N regions show higher mean values ($\log \sigma/\text{km s}^{-1} \sim 1.56$ for both cuts and $\log \text{SFE}/\text{Myr}^{-1} = -2.41 \pm 0.44$ for cut on Σ_{H_2} and $\log \text{SFE}/\text{Myr}^{-1} = -2.10 \pm 0.40$ on Σ_{SFR}) than the low-N regions ($\log \sigma/\text{km s}^{-1} \sim 1.30$ and $\log \text{SFE}/\text{Myr}^{-1} \sim -2.62$ for

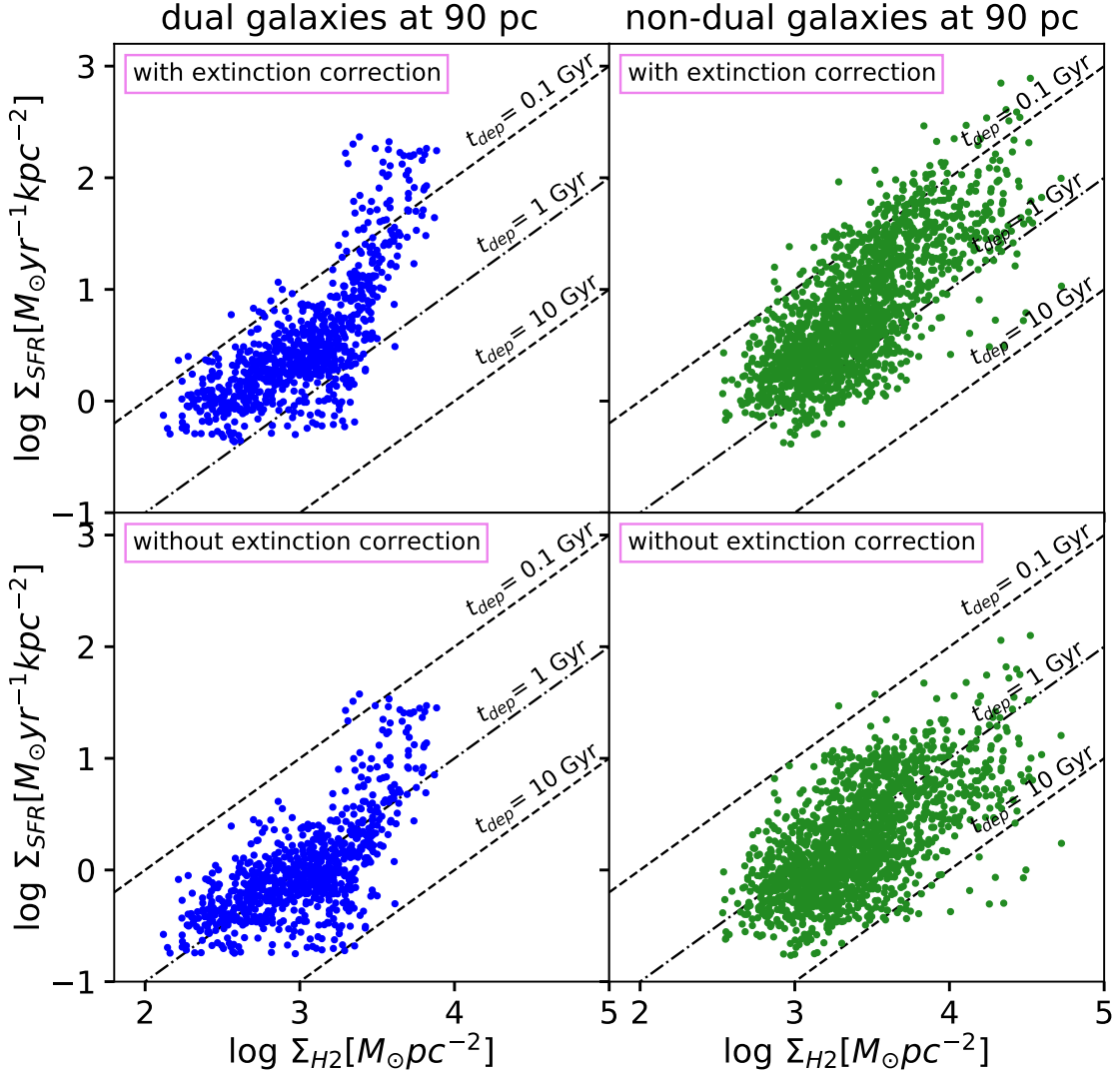


Fig. 4. *Left panels:* KS relation of galaxies with two branches, taking into account the extinction correction (*top*) and without this correction (*bottom*). *Right panels:* the same for the non-dual galaxies.

Table 5. Spearman rank correlation coefficients

	t_{dep} vs. b		SFE vs. σ	
	ρ_s	p-value	ρ_s	p-value
dual	-0.26	6.13e-17	-0.08	0.01
high-N (cut on Σ_{H2})	-0.38	2.79e-14	0.32	5.79e-7
low-N (cut on Σ_{H2})	-0.18	4.12e-6	-	-
high-N (cut on Σ_{SFR})	-0.48	2.51e-10	0.13	0.16
low-N (cut on Σ_{SFR})	-0.15	1.22e-5	-	-
non-dual	-0.13	9.78e-8	0.02	0.34

Notes. Spearman ρ_{sp} rank correlation coefficients (two-sided p-values). We exclude upper limits from the analysis. We consider the correlations are statistically significant when $\rho_{sp} \gtrsim 0.3$ and p-value $< 3\%$.

both cuts). Also, for the high-N regions, the SFE increases with increasing σ , though the scatter is large (~ 2 dex).

The high-N regions are located in the central regions of the four dual objects, so we also investigate if the central regions of the non-dual galaxies have different SFE and/or σ . To do this, we consider the regions at radii < 500 pc, which is where most of the high-N regions are located in the dual galaxies (see Sect. 4.3). As opposed to the dual galaxies, we find that for the non-dual

galaxies, the internal ($r < 500$ pc) and external regions have similar mean SFE ($\log \text{SFE}/\text{Myr}^{-1} = -2.48 \pm 0.34$ and -2.66 ± 0.28 for the internal and external regions respectively) and just slightly higher σ ($\log \sigma/\text{km s}^{-1} = 1.53 \pm 0.18$ and 1.36 ± 0.16 , respectively).

The large scatter at these scales may be due to the fact that we can resolve individual regions, obtaining information from the clouds in different evolutionary phases (Kruijssen & Long-

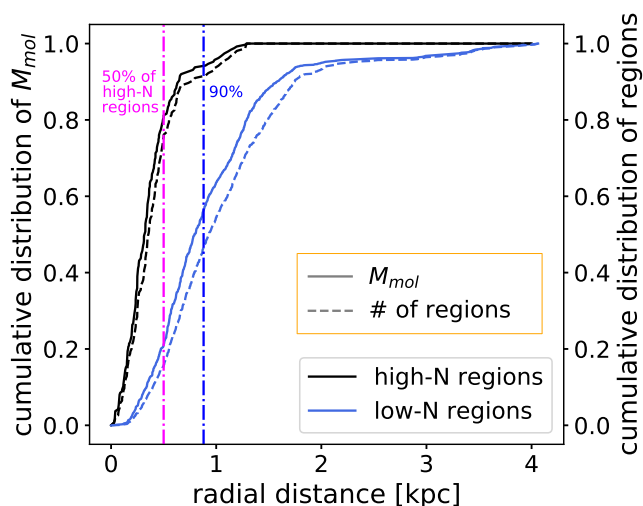


Fig. 5. Cumulative distribution of the molecular mass (*left vertical axis* and solid lines) of the 90 pc regions in the dual galaxies, selected applying a cut on Σ_{H_2} , as a function of the radial distance. The dashed lines (*right vertical axis*) show the cumulative distribution of the number of regions in each branch. Colours are as in Fig. 1. The dash-dot lines correspond to the radii that include a percentage of regions.

more 2014). Several SF models suggest that the dynamical state of the cloud, and not only its density, affects its ability to collapse and form stars (e.g., Krumholz & McKee 2005; Hennebelle & Chabrier 2011; Federrath & Klessen 2013). These models focus on the properties of turbulent molecular clouds, proposing that the supersonic and compressive turbulence induces the formation of stars. In this case, we would expect the SFE to increase with increasing gas velocity dispersion (Orkisz et al. 2017). This is consistent with our findings for the high-N regions in the dual galaxies. Cloud-cloud collisions could be enhanced near the location of the bar resonances in the central regions of these galaxies (Sánchez-García et al. in prep). These collisions could result in an increased turbulence, which may induce a greater compression of the gas (increasing its density), and finally lead to an enhanced star formation. Moreover, the increase in gas density compensates for the high turbulence, causing, together, b to increase in these central regions.

5. Conclusions

We have presented a high-resolution study of the star-formation relation in a sample of 16 local LIRGs on spatial scales of ~ 90 pc. We have combined the SFR calculated from the HST/NICMOS Paa emission with cold molecular gas from ALMA CO(2–1) data to probe the star-formation relations.

We find that four galaxies from our sample show a dual behaviour in their KS relation at 90 pc scales. The regime with higher gas and SFR surface densities is characterized by a steeper power-law index in the central region of the galaxies ($r < 0.85$ kpc). The other regime, which shows lower values of gas and SFR surface densities, is located in the more external disk regions. This dual behaviour disappears at large spatial scales (240 and 500 pc).

The gas in the central region of the dual galaxies shows greater turbulence (higher σ) and slightly stronger self-gravity (higher b) than the external region. These dynamical conditions of the gas might lead to more efficient star formation in the central region. The rest of the galaxies do not show a clear trend be-

tween these two parameters. These variations within each galaxy and among the galaxies of the sample suggest that the local dynamical environment plays a role in the star formation process. The fraction of AGN and bars is similar for dual and non-dual galaxies, although a larger sample is needed to evaluate their impact on the SF law at 90 pc scale.

Acknowledgements. We thank referee for the useful comments and suggestions. MSG acknowledges support from the Spanish Ministerio de Economía y Competitividad through the grants BES-2016-078922, ESP2017-83197-P. LC and MSG acknowledge support from the research project PID2019-106280GB-I00. MPS acknowledges support from the Comunidad de Madrid through the Atracción de Talento Investigador Grant 2018-T1/TIC-11035 and PID2019-105423GA-I00 (MCIU/AEI/FEDER,UE). SGB and AAH acknowledge support from PGC2018-094671-B-I00 (MCIU/AEI/FEDER,UE). SGB acknowledges support from the research project PID2019-106027GA-C44 of the Spanish Ministerio de Ciencia e Innovación. JPL acknowledges support from PID2019-105423GA-I00. EB acknowledges the support from Comunidad de Madrid through the Atracción de Talento grant 2017-T1/TIC-5213. SC acknowledge financial support from the State Agency for Research of the Spanish MCIU through the ‘Centre of Excellence Severo Ochoa’ award to the Instituto de Astrofísica de Andalucía (SEV-2017-0709). AL acknowledges the support from Comunidad de Madrid through the Atracción de Talento Investigador Grant 2017-T1/TIC-5213, and PID2019-106280GB-I00 (MCIU/AEI/FEDER,UE) This paper makes use of the following ALMA data: ADS/JAO.ALMA#2017.1.00255.S, ADS/JAO.ALMA#2013.1.00271.S, ADS/JAO.ALMA#2013.1.00243.S, ADS/JAO.ALMA#2015.1.00714.S and ADS/JAO.ALMA#2017.1.00395.S. ALMA is a partnership of ESO (representing its member states), NSF (USA) and NINS (Japan), together with NRC (Canada) and NSC and ASIAA (Taiwan) and KASI (Republic of Korea), in cooperation with the Republic of Chile. The Joint ALMA Observatory is operated by ESO, AUI/NRAO and NAOJ. The National Radio Astronomy Observatory is a facility of the National Science Foundation operated under cooperative agreement by Associated Universities, Inc.

References

- Accurso, G., Saintonge, A., Catinella, B., et al. 2017, *MNRAS*, 470, 4750
 Albrecht, M., Krügel, E., & Chini, R. 2007, *A&A*, 462, 575
 Alonso-Herrero, A., García-Marín, M., Monreal-Ibero, A., et al. 2009, *A&A*, 506, 1541
 Alonso-Herrero, A., Pereira-Santaella, M., Rieke, G. H., & Rigopoulou, D. 2012, *ApJ*, 744, 2
 Alonso-Herrero, A., Rieke, G. H., Rieke, M. J., et al. 2006, *ApJ*, 650, 835
 Bellocchi, E., Arribas, S., Colina, L., & Miralles-Caballero, D. 2013, *A&A*, 557, A59
 Böker, T., Calzetti, D., Sparks, W., et al. 1999, *ApJS*, 124, 95
 Bolatto, A. D., Wolfire, M., & Leroy, A. K. 2013, *ARA&A*, 51, 207
 Briggs, D. S. 1995, in *American Astronomical Society Meeting Abstracts*, Vol. 187, American Astronomical Society Meeting Abstracts, 112.02
 Casasola, V., Hunt, L., Combes, F., & García-Burillo, S. 2015, *A&A*, 577, A135
 Corbett, E. A., Kewley, L., Appleton, P. N., et al. 2003, *ApJ*, 583, 670
 Daddi, E., Elbaz, D., Walter, F., et al. 2010, *ApJ*, 714, L118
 Downes, D. & Solomon, P. M. 1998, *ApJ*, 507, 615
 Federrath, C. & Klessen, R. S. 2013, *ApJ*, 763, 51
 Fitzpatrick, E. L. 1999, *PASP*, 111, 63
 Friedman, J. H. 1991, *The Annals of Statistics*, 19, 1
 Garay, G., Mardones, D., & Mirabel, I. F. 1993, *A&A*, 277, 405
 García-Burillo, S., Usero, A., Alonso-Herrero, A., et al. 2012, *A&A*, 539, A8
 Genzel, R., Tacconi, L. J., Gracia-Carpio, J., et al. 2010, *MNRAS*, 407, 2091
 Hennebelle, P. & Chabrier, G. 2011, *ApJ*, 743, L29
 Hummer, D. G. & Storey, P. J. 1987, *MNRAS*, 224, 801
 Kennicutt, R. C. & Evans, N. J. 2012, *ARA&A*, 50, 531
 Kennicutt, Jr., R. C. 1998, *ApJ*, 498, 541
 Kewley, L. J., Dopita, M. A., Sutherland, R. S., Heisler, C. A., & Trevena, J. 2001, *ApJ*, 556, 121
 Kreckel, K., Faesi, C., Kruijssen, J. M. D., et al. 2018, *ApJ*, 863, L21
 Kroupa, P. 2001, *MNRAS*, 322, 231
 Kruijssen, J. M. D. & Longmore, S. N. 2014, *MNRAS*, 439, 3239
 Krumholz, M. R. & McKee, C. F. 2005, *ApJ*, 630, 250
 Leroy, A. K., Schinnerer, E., Hughes, A., et al. 2017, *ApJ*, 846, 71
 Leroy, A. K., Walter, F., Brinks, E., et al. 2008, *AJ*, 136, 2782
 Leroy, A. K., Walter, F., Sandstrom, K., et al. 2013, *AJ*, 146, 19
 Lipari, S., Díaz, R., Taniguchi, Y., et al. 2000, *AJ*, 120, 645

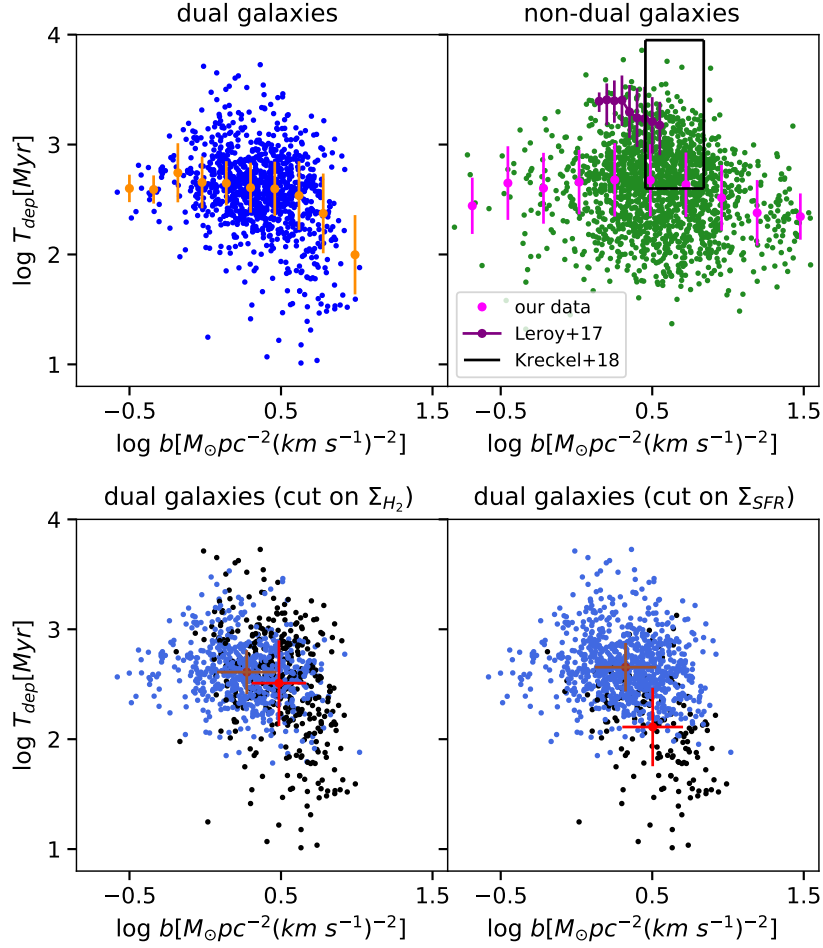


Fig. 6. Cold molecular gas depletion time, t_{dep} , as a function of the self-gravity of the regions (parameter b) at 90 pc scales for the dual (*top left*) and the non-dual galaxies (*top right*). The orange and magenta circles show the median t_{dep} in bins of b . The errorbars indicate the mean absolute deviation of the points in the bins. We show in purple the values of these parameters estimated in M51 (Leroy+17) and the open black rectangle represents the range of values in NGC 628 (Kreckel+18). The black and blue circles correspond to regions in the high- and low-N regimes, respectively, for the four dual objects (*bottom row*). The red and brown lines indicate mean the mean absolute deviation (MAD) for the regions in high- and low-N regimes, respectively.

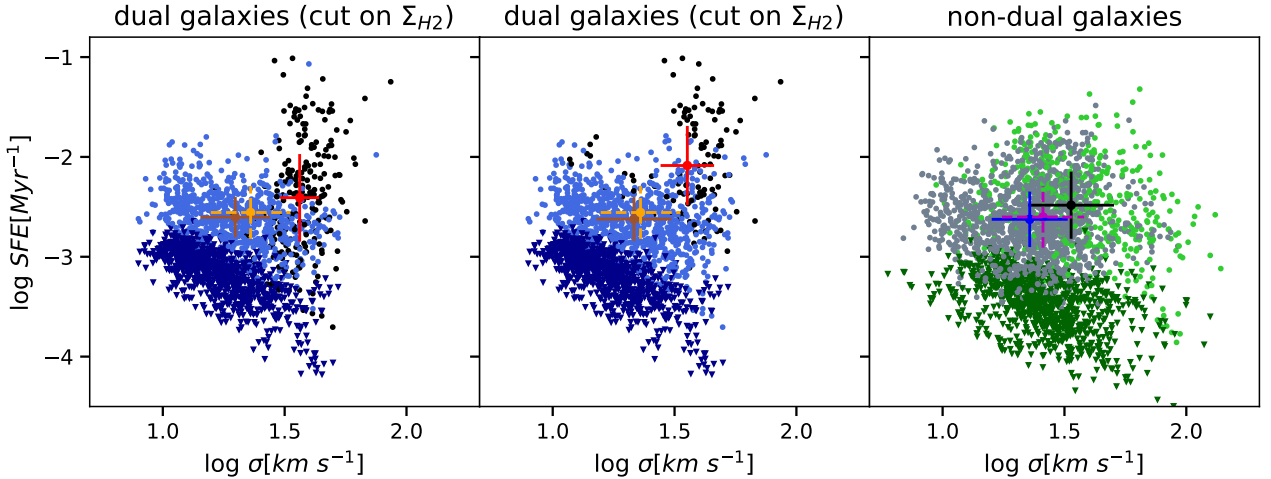


Fig. 7. SF efficiency of the molecular gas, as a function of the velocity dispersion of the gas (σ) at 90 pc scales. The *left* and *middle* panels correspond to the cut on Σ_{H_2} and Σ_{SFR} axis for each galaxy, respectively. Colours are as in previous figures. The red and brown points indicate the mean and mean absolute deviation (MAD) for the regions in high- and low-N regimes, respectively. *Right* panel: Similar to the *left* and *middle* panels but for non-dual galaxies. The central regions ($r < 0.50$ kpc) are represented in green and the more external regions in grey. The black and blue points correspond to the mean and MAD value of the central and external regions, respectively. The orange and magenta points are the mean and MAD for all the regions of each panel. The inverted triangles indicate upper limits.

- McMullin, J. P., Waters, B., Schiebel, D., Young, W., & Golap, K. 2007, in *Astronomical Society of the Pacific Conference Series*, Vol. 376, *Astronomical Data Analysis Software and Systems XVI*, ed. R. A. Shaw, F. Hill, & D. J. Bell, 127
- Onodera, S., Kuno, N., Tosaki, T., et al. 2010, *ApJ*, 722, L127
- Orkisz, J. H., Pety, J., Gerin, M., et al. 2017, *A&A*, 599, A99
- Osterbrock, D. E. & Ferland, G. J. 2006, *Astrophysics of gaseous nebulae and active galactic nuclei*
- Papadopoulos, P. P., van der Werf, P., Xilouris, E., Isaak, K. G., & Gao, Y. 2012, *ApJ*, 751, 10
- Paraficz, D., Rybak, M., McKean, J. P., et al. 2018, *A&A*, 613, A34
- Pereira-Santaella, M., Alonso-Herrero, A., Santos-Lleo, M., et al. 2011, *A&A*, 535, A93
- Pereira-Santaella, M., Colina, L., García-Burillo, S., et al. 2016a, *A&A*, 594, A81
- Pereira-Santaella, M., Colina, L., García-Burillo, S., et al. 2021, *A&A*, 651, A42
- Pereira-Santaella, M., Colina, L., García-Burillo, S., et al. 2016b, *A&A*, 587, A44
- Pereira-Santaella, M., Diamond-Stanic, A. M., Alonso-Herrero, A., & Rieke, G. H. 2010, *ApJ*, 725, 2270
- Pessa, I., Schinnerer, E., Belfiore, F., et al. 2021, *A&A*, 650, A134
- Petric, A. O., Armus, L., Howell, J., et al. 2011, *ApJ*, 730, 28
- Piqueras López, J., Colina, L., Arribas, S., & Alonso-Herrero, A. 2013, *A&A*, 553, A85
- Rich, J. A., Torrey, P., Kewley, L. J., Dopita, M. A., & Rupke, D. S. N. 2012, *ApJ*, 753, 5
- Saito, T., Iono, D., Xu, C. K., et al. 2016, *PASJ*, 68, 20
- Sánchez, S. F., Rosales-Ortega, F. F., Iglesias-Páramo, J., et al. 2014, *A&A*, 563, A49
- Sanders, D. B., Mazzarella, J. M., Kim, D. C., Surace, J. A., & Soifer, B. T. 2003, *AJ*, 126, 1607
- Schmidt, M. 1959, *ApJ*, 129, 243
- Schruba, A., Leroy, A. K., Walter, F., Sandstrom, K., & Rosolowsky, E. 2010, *ApJ*, 722, 1699
- Sun, J., Leroy, A. K., Schruba, A., et al. 2018, *ApJ*, 860, 172
- van den Broek, A. C., van Driel, W., de Jong, T., et al. 1991, *A&AS*, 91, 61
- Veilleux, S., Kim, D. C., Sanders, D. B., Mazzarella, J. M., & Soifer, B. T. 1995, *ApJS*, 98, 171
- Viaene, S., Forbrich, J., & Fritz, J. 2018, *MNRAS*, 475, 5550
- Williams, T. G., Gear, W. K., & Smith, M. W. L. 2018, *MNRAS*, 479, 297
- Xu, C. K., Cao, C., Lu, N., et al. 2015, *ApJ*, 799, 11
- Yao, L., Seaquist, E. R., Kuno, N., & Dunne, L. 2003, *ApJ*, 597, 1271
- Yuan, T. T., Kewley, L. J., & Sanders, D. B. 2010, *ApJ*, 709, 884

Appendix A: Figures

Appendix A.1: Star formation relation for individual galaxies and CO(2–1) maps and HST/NICMOS images

In this appendix we present the KS relations, the regions considered in this work, the ALMA CO(2–1) maps and the HST/NICMOS Pa α images for the whole sample.

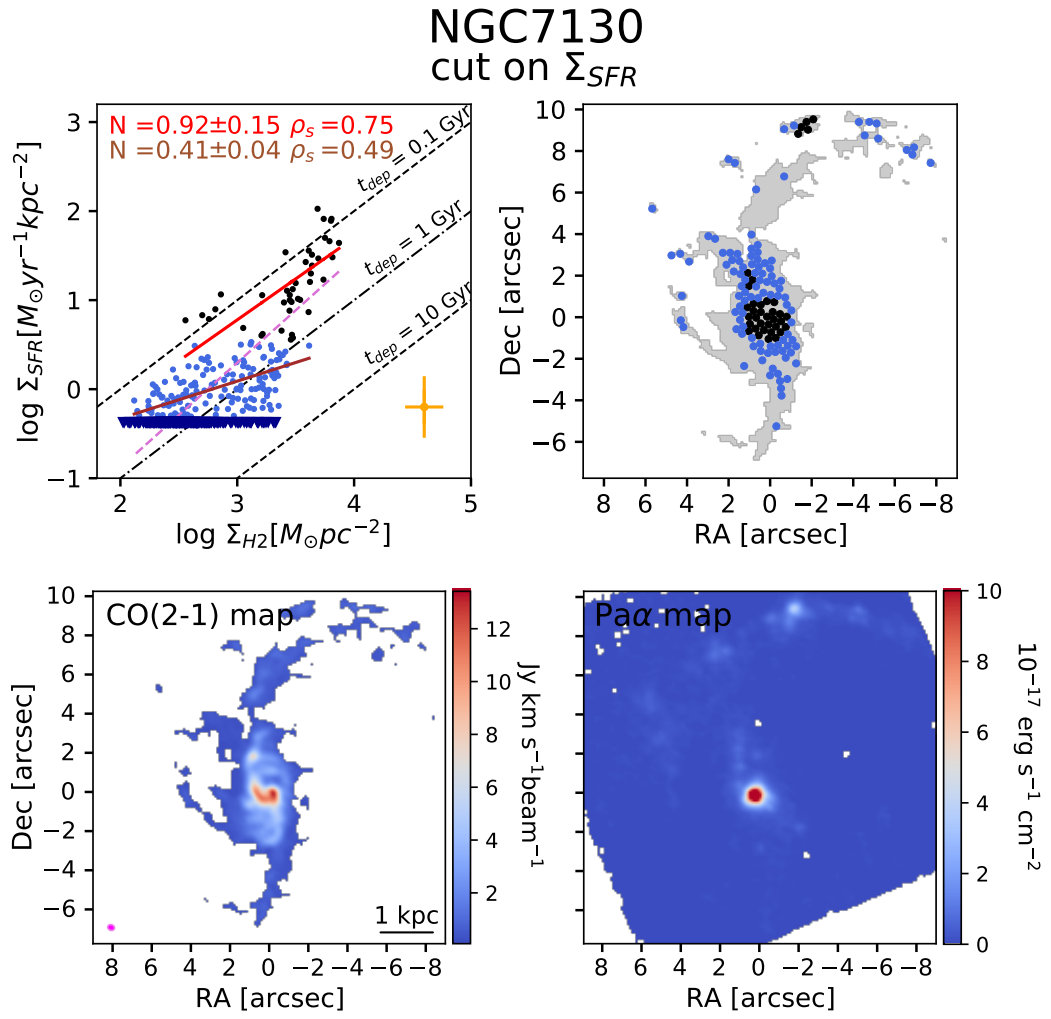
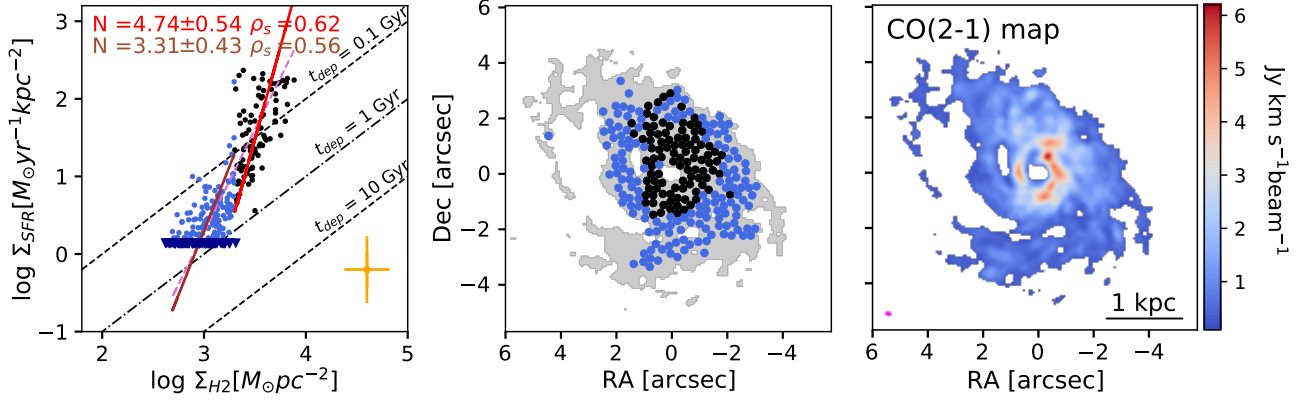


Fig. A.1. *Top panels:* Same as Fig. 1, applying the MARS method to the $\log_{10}\Sigma_{H_2}$. *Bottom panels:* ALMA CO(2–1) (*left*) and HST/NICMOS Pa α maps (*right*). This last map is smoothed to the ALMA resolution. The magenta filled ellipse (*bottom left*) represents the beam size ($0''.36 \times 0''.29$ PA=69°).

NGC1614

cut on Σ_{H_2}


NGC1614

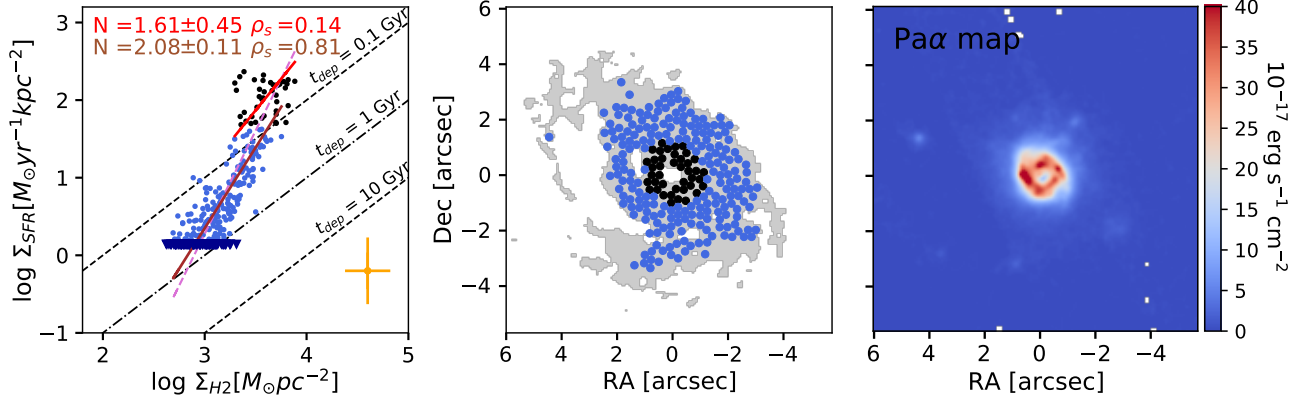
cut on Σ_{SFR}


Fig. A.2. Same as Fig. 1, applying the MARS method to the $\log_{10}\Sigma_{H_2}$ (top left and middle) and $\log_{10}\Sigma_{SFR}$ (bottom left and middle). Right panels: ALMA CO(2–1) (top) and HST/NICMOS Paα maps (bottom). This last map is smoothed to the ALMA resolution. The magenta filled ellipse represents the beam size.

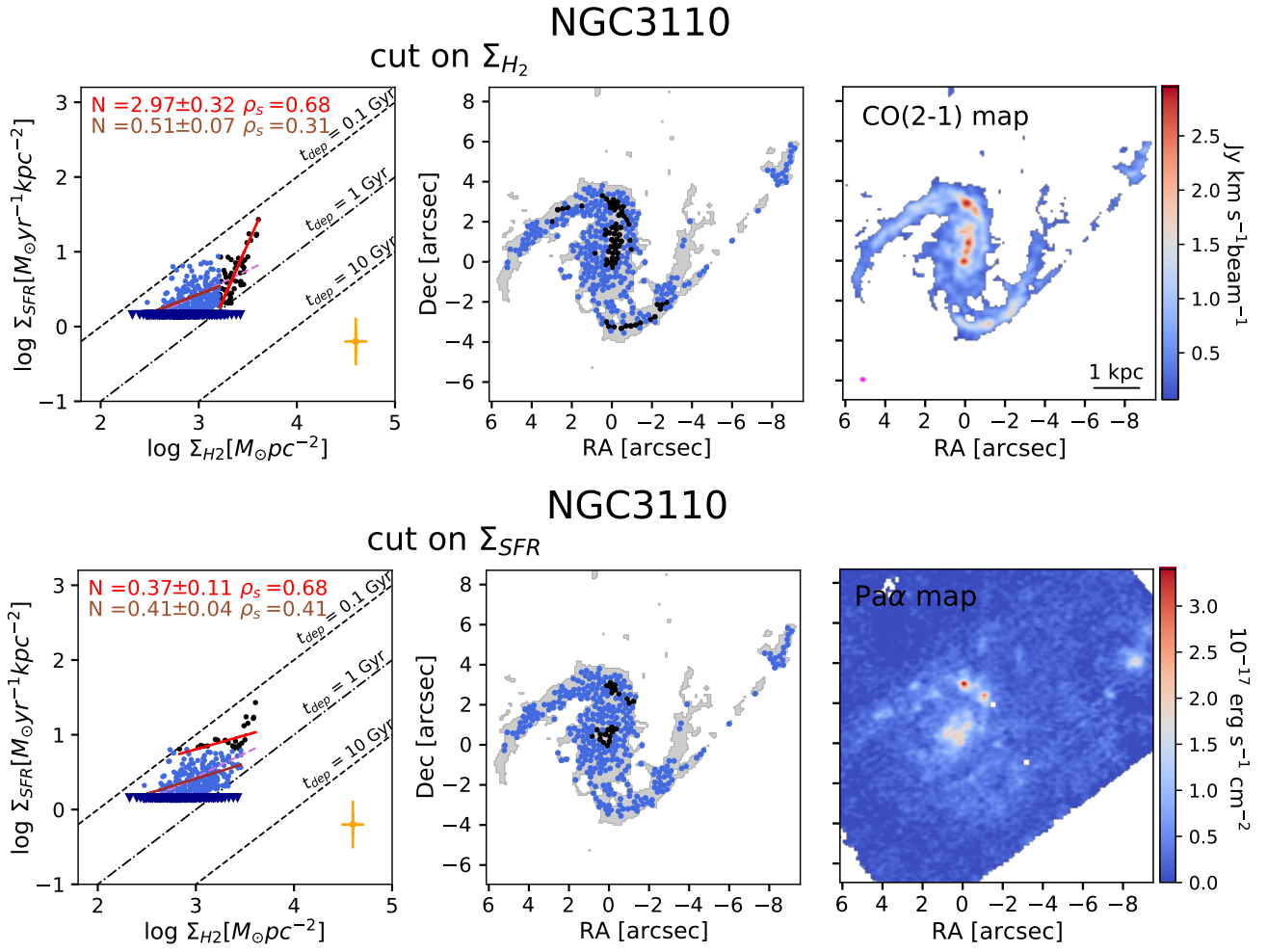


Fig. A.2. Continued.

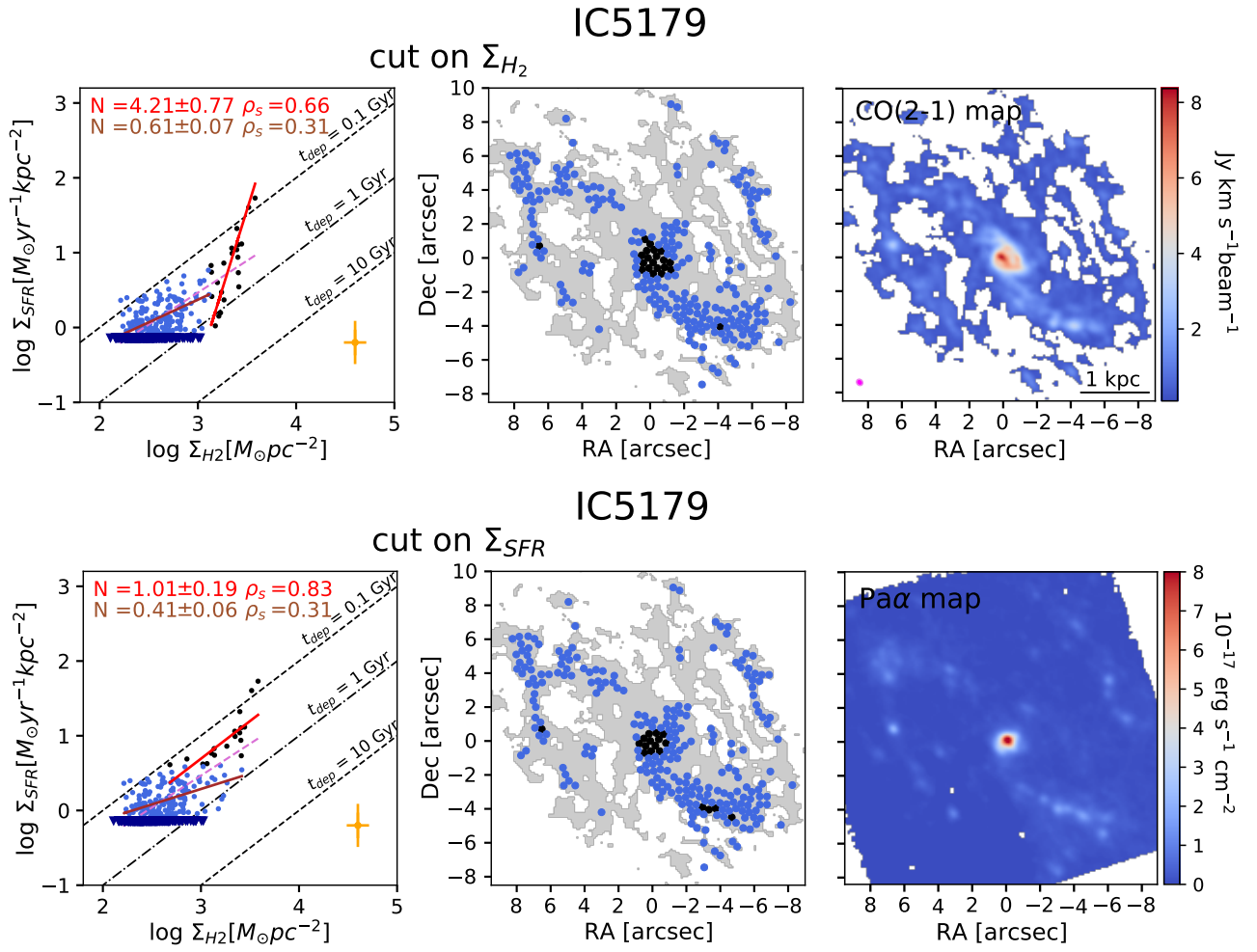


Fig. A.2. Continued.

ESO297-G011

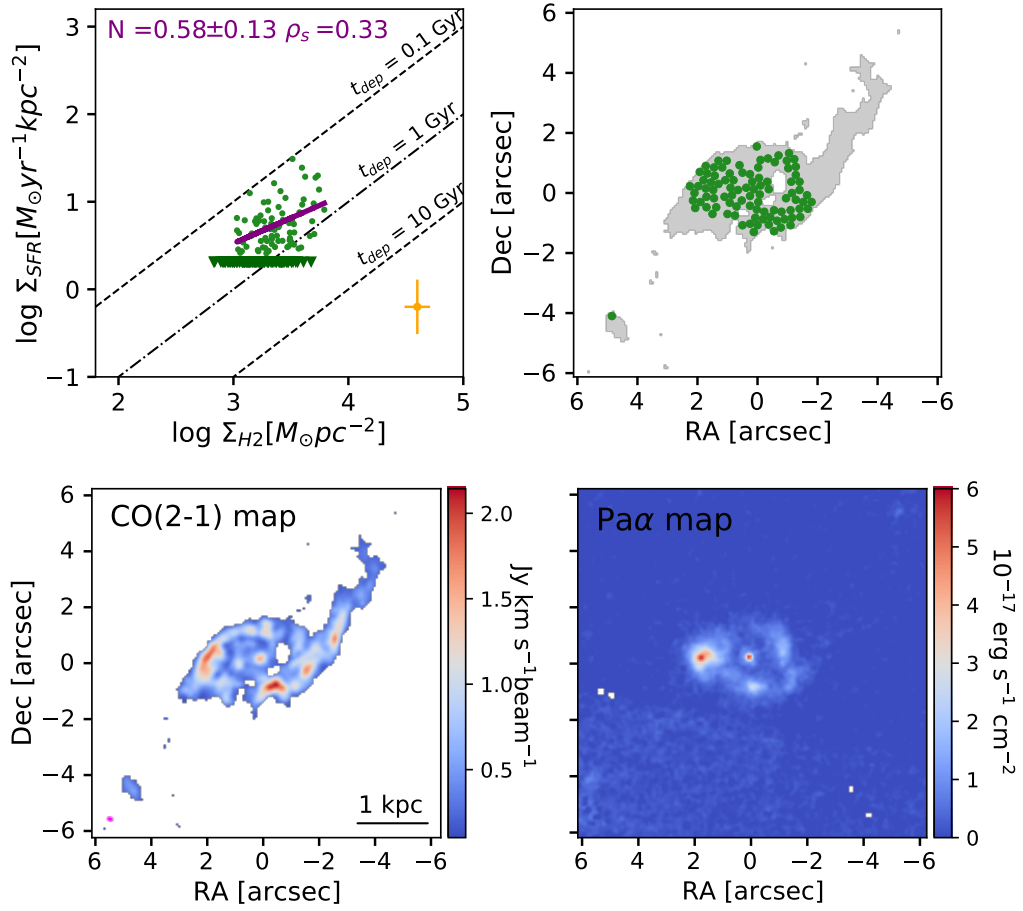


Fig. A.3. *Top left* panel: SFR surface density (Σ_{SFR}) as a function of the molecular gas surface density (Σ_{H_2}) for the non dual galaxies of the sample using 90 pc regions. The green circles indicate data points in each galaxy. The solid purple line indicates the best fit. The Spearman's rank correlation coefficients (ρ_s) and the power-law index (N) of the derived best-fits KS relation are reported in the figure. The dashed lines mark constant t_{dep} values. *Top right*: Location of the regions on the CO(2–1) map (grey). *Bottom* panels: ALMA CO(2–1) (*left*) and HST/NICMOS Pa α (*right*) maps.

NGC2369

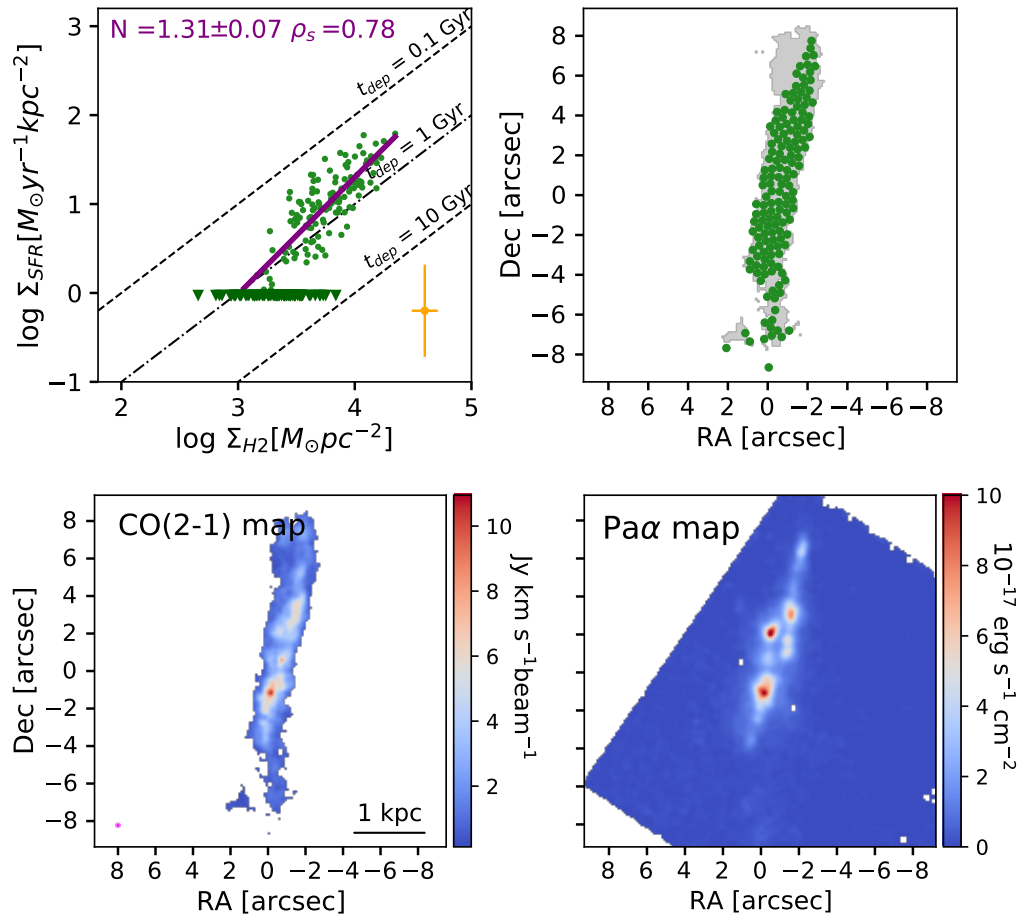


Fig. A.3. Continued.

NGC3256

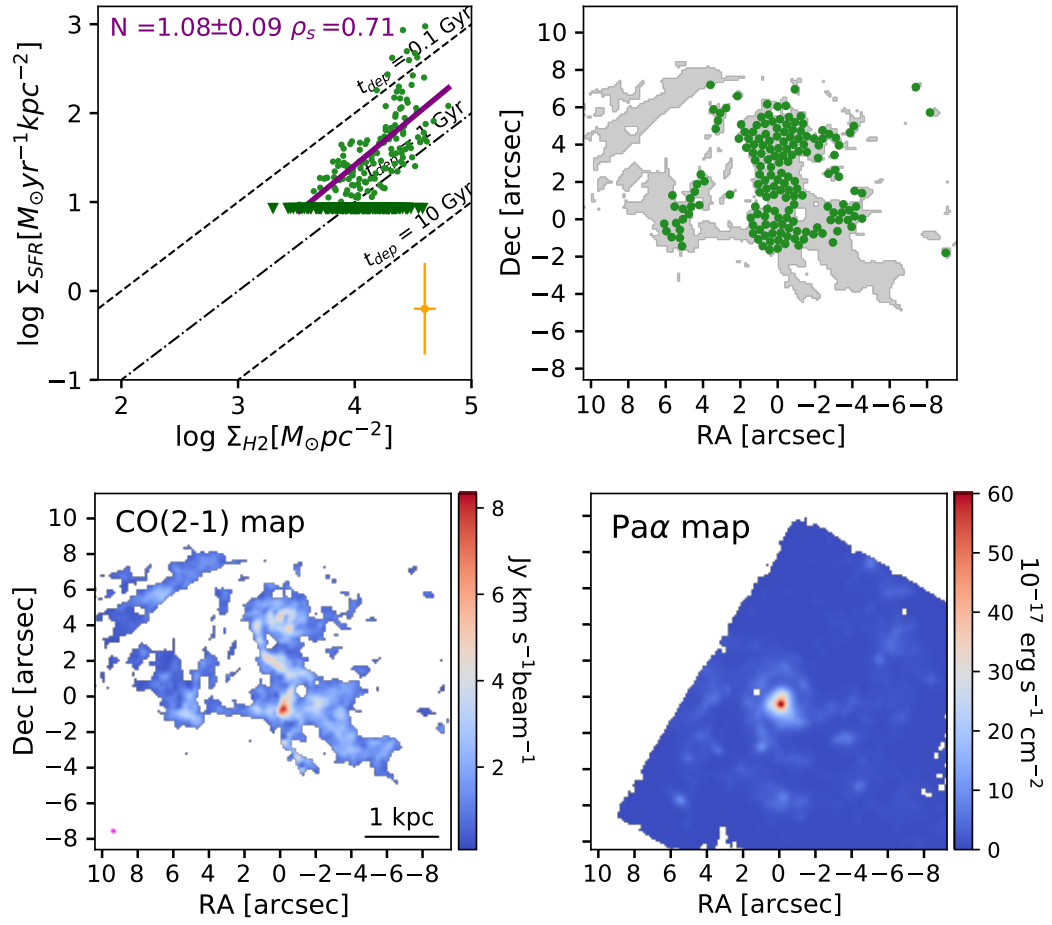


Fig. A.3. Continued.

ESO320-G030

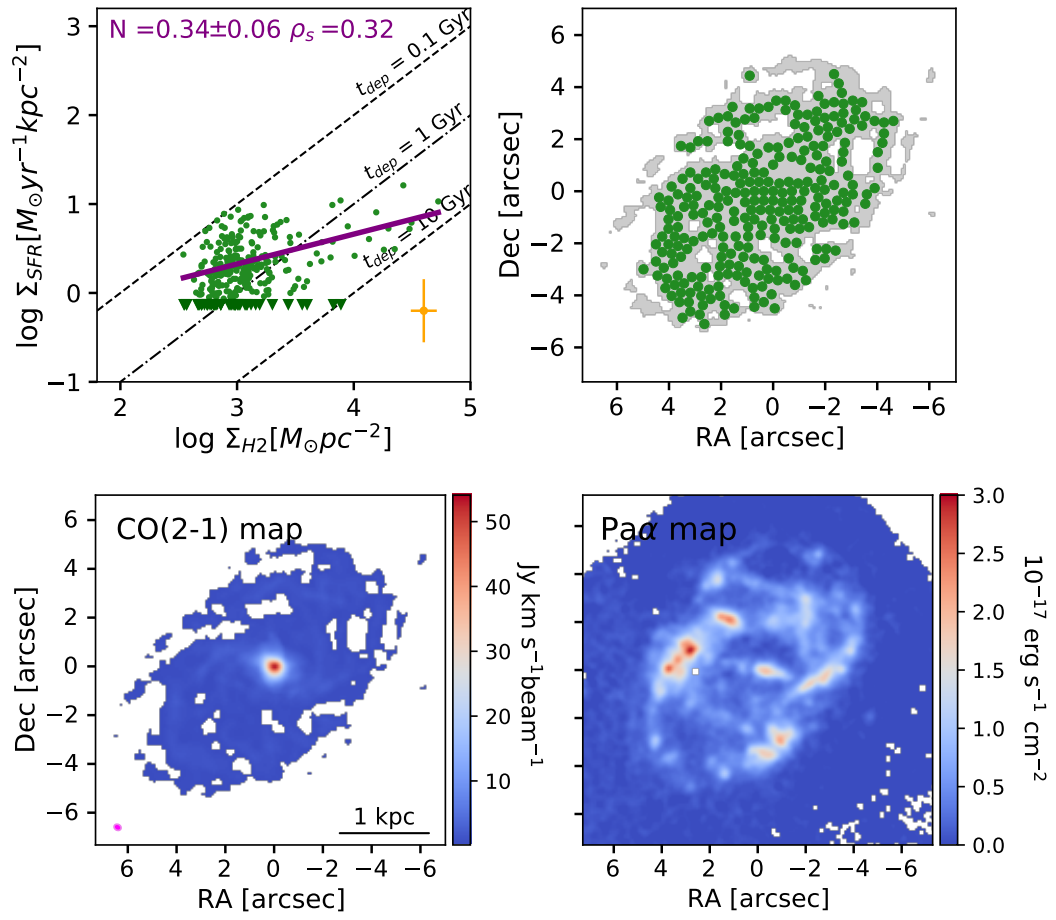


Fig. A.3. Continued.

MCG-02-33-098-W

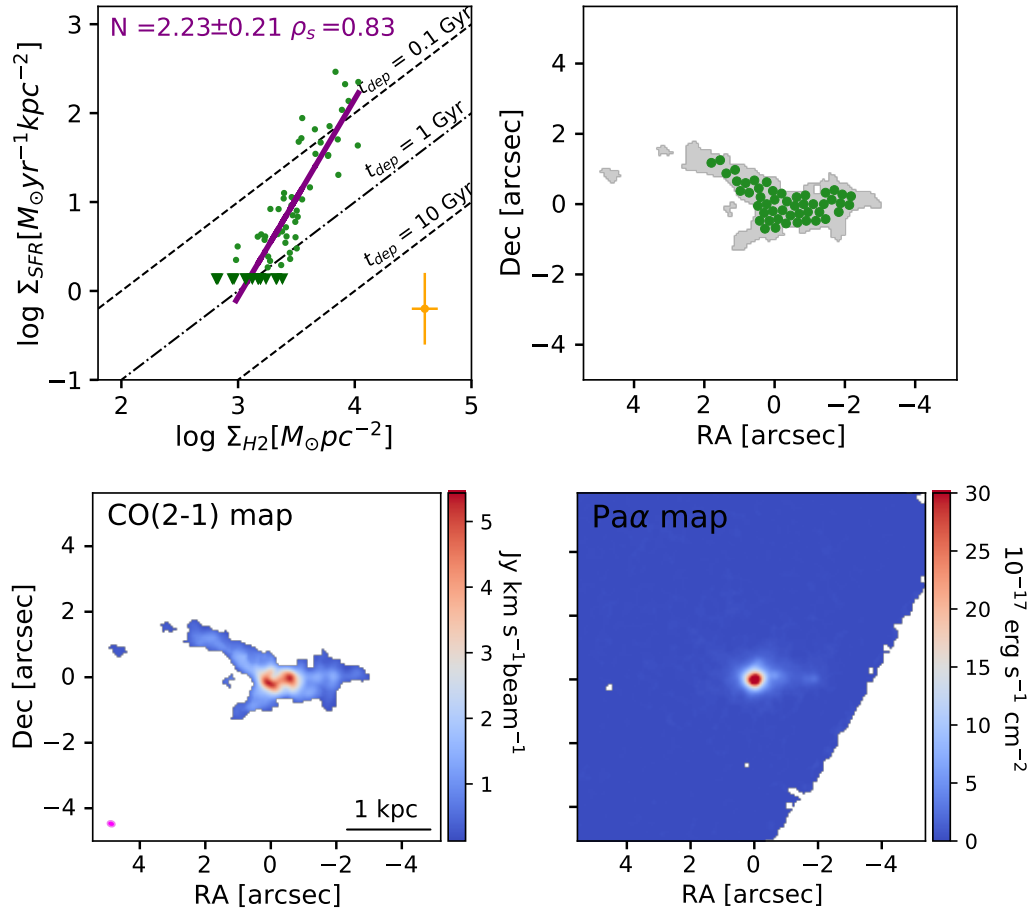


Fig. A.3. Continued.

MCG-02-33-098-E

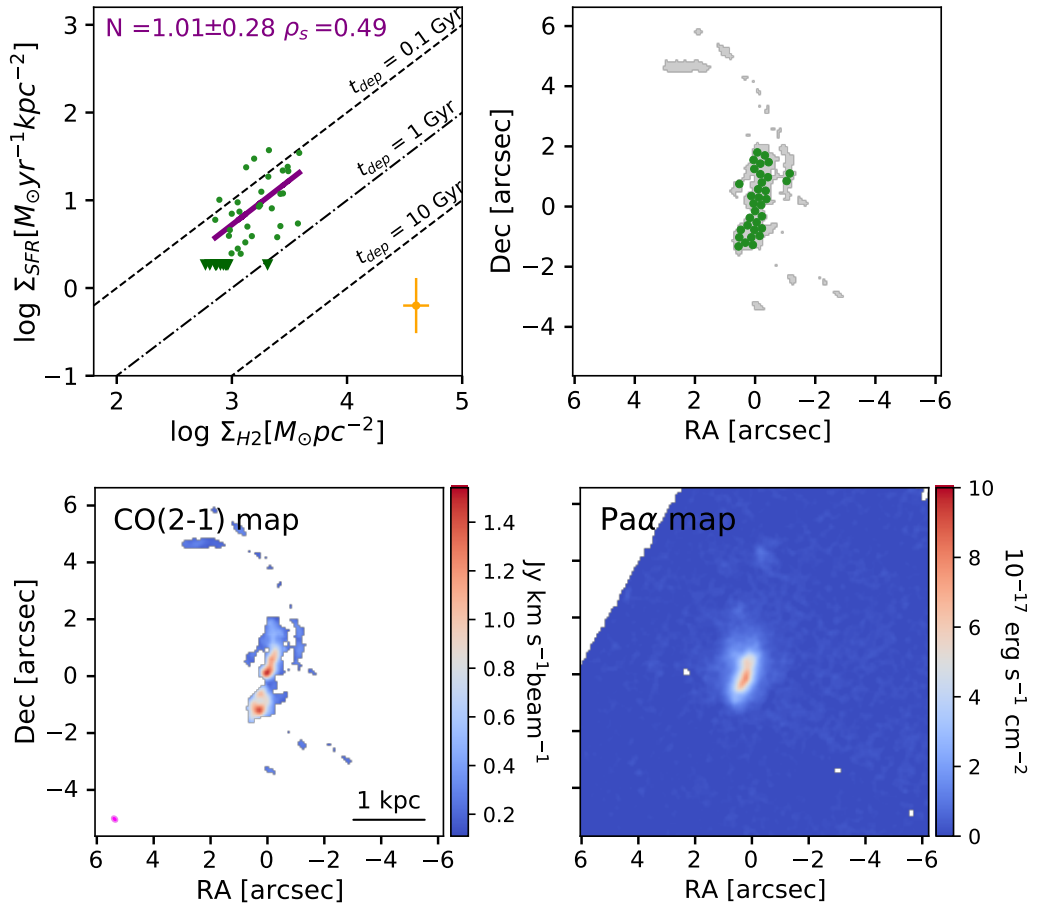


Fig. A.3. Continued.

NGC5135

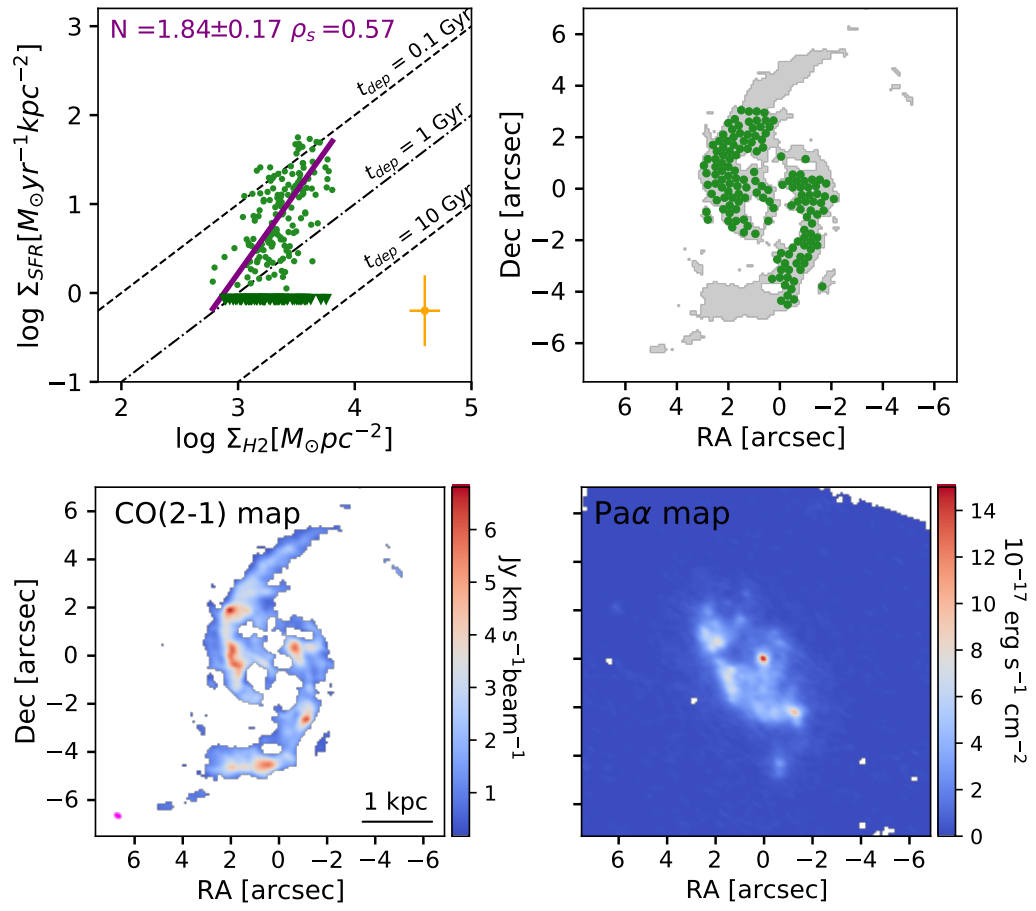


Fig. A.3. Continued.

IC4518W

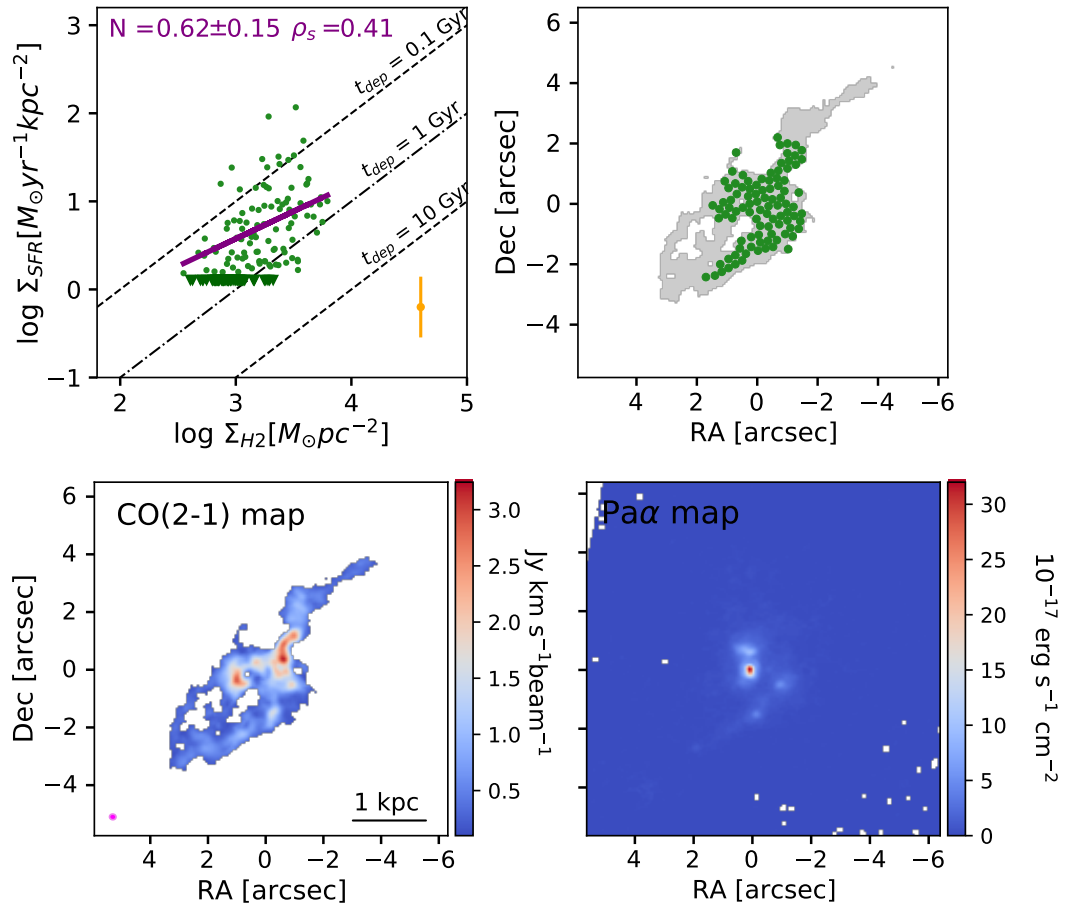


Fig. A.3. Continued.

IC4518E

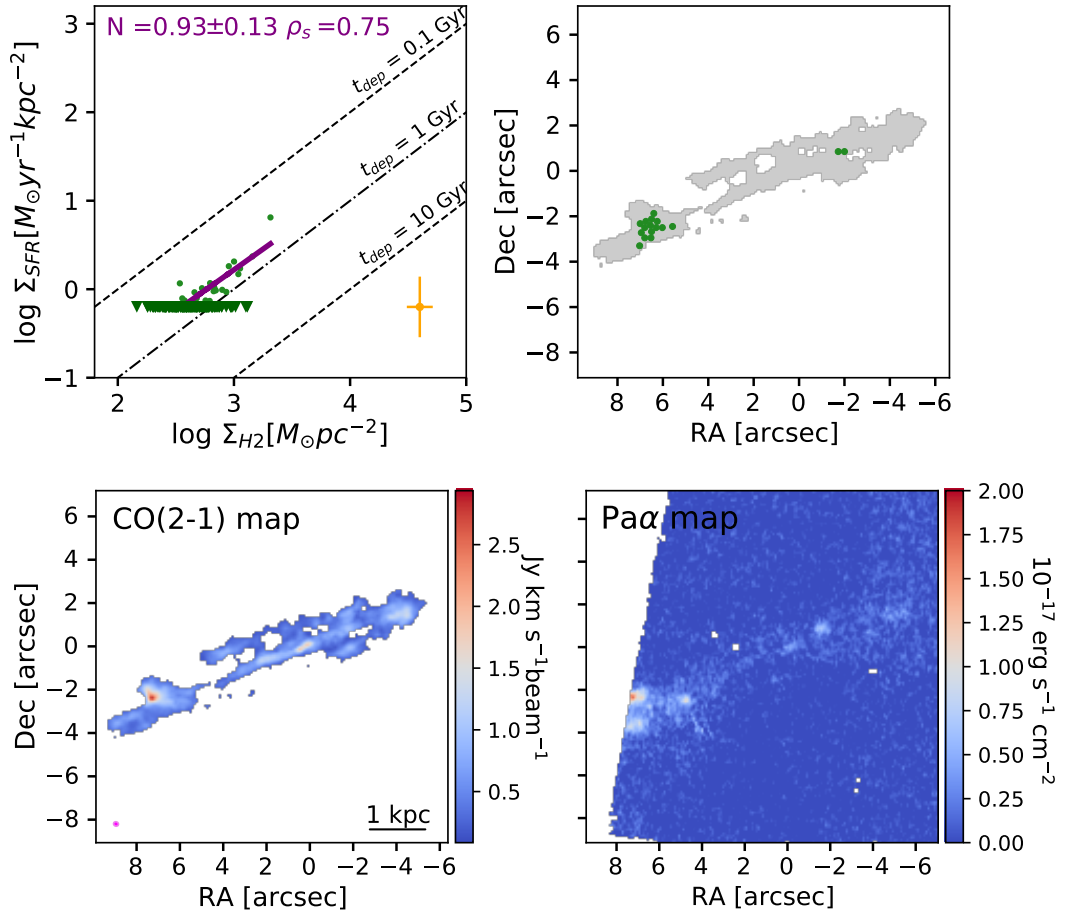


Fig. A.3. Continued.

IRASF17138-1017

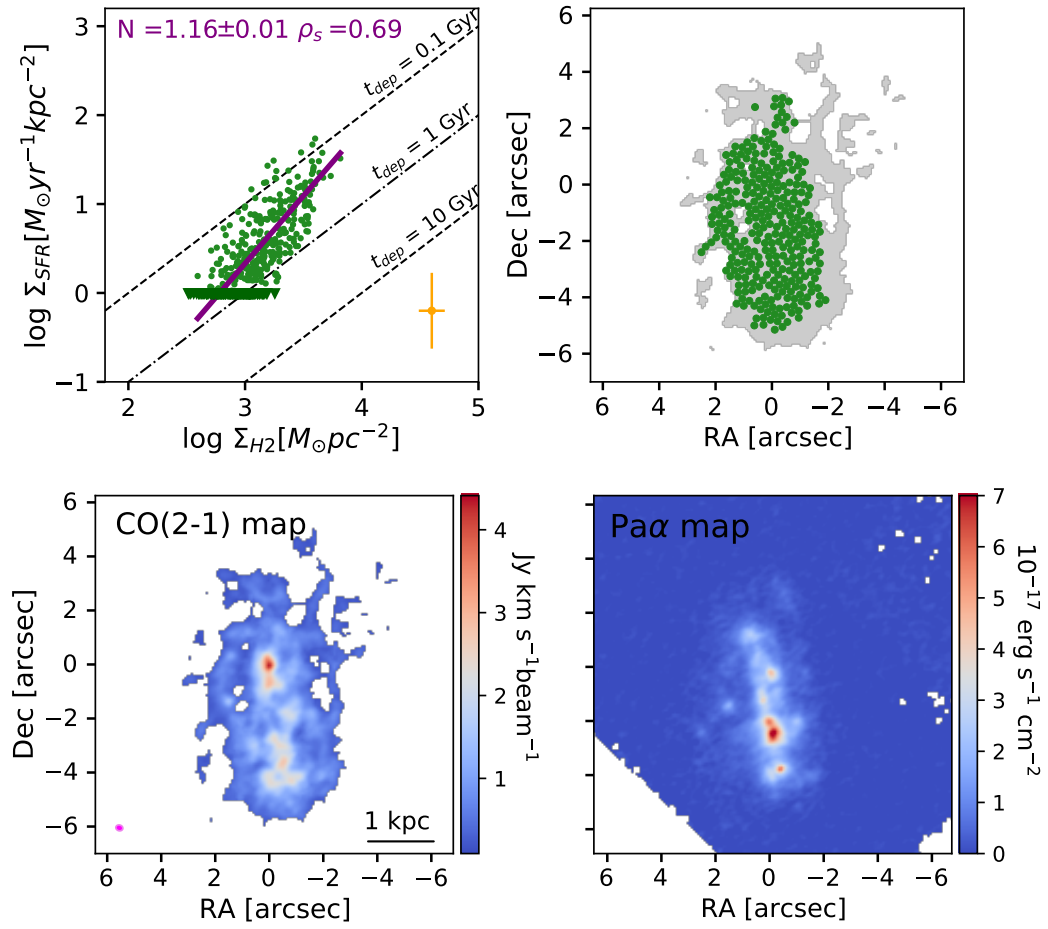


Fig. A.3. Continued.

IC4734

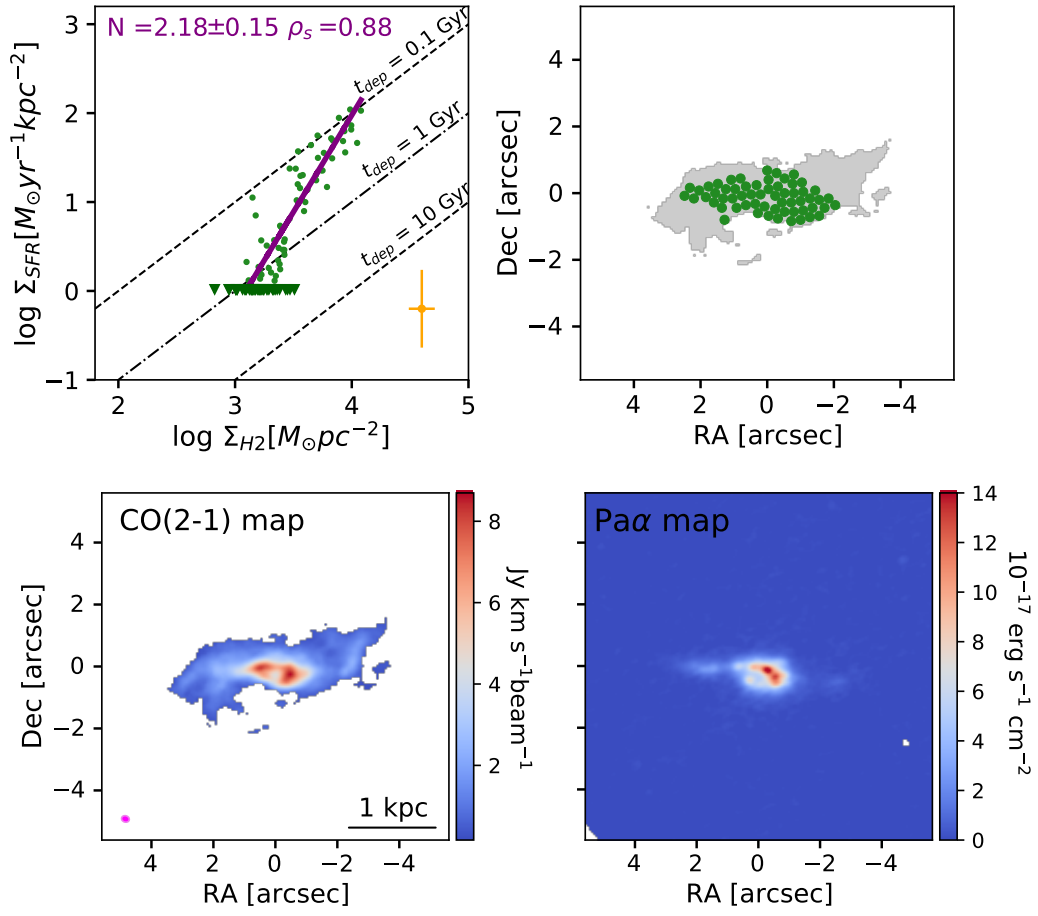


Fig. A.3. Continued.

NGC7469

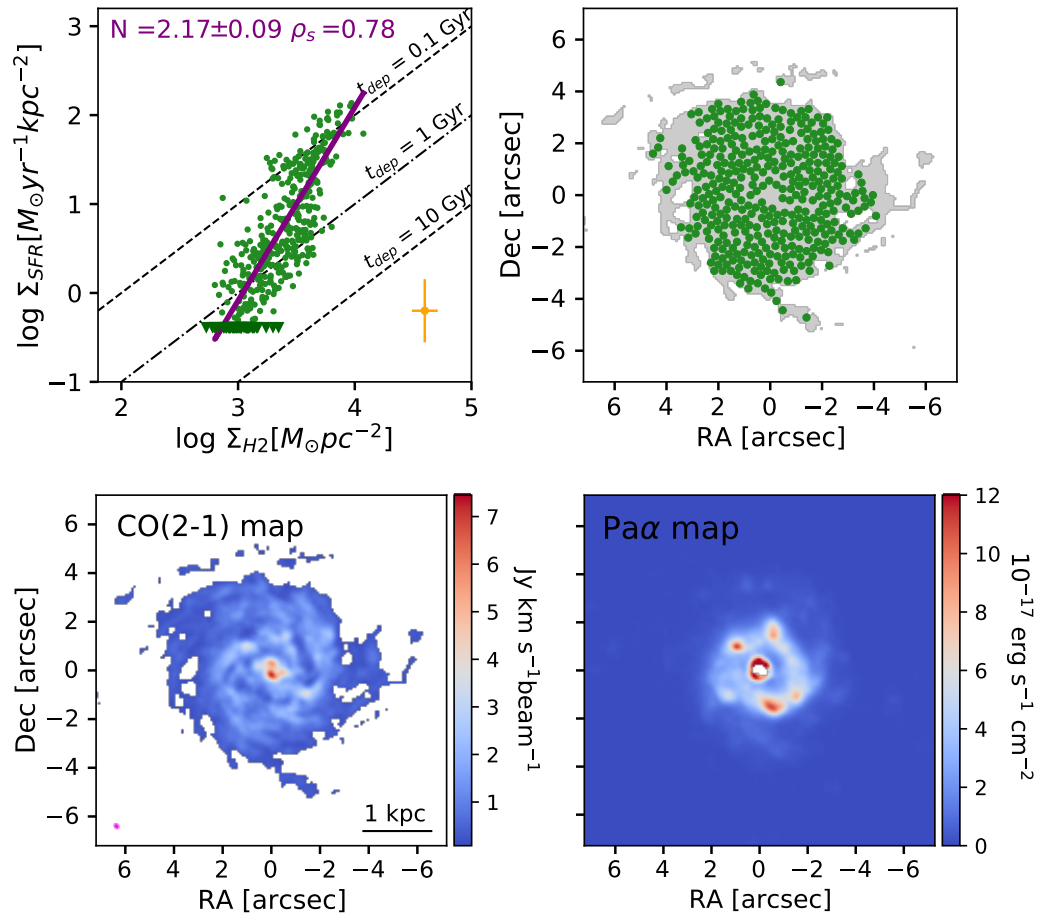


Fig. A.3. Continued.